



#### Available online at www.sciencedirect.com

# **ScienceDirect**

Geochimica et Cosmochimica Acta

Geochimica et Cosmochimica Acta 273 (2020) 291-312

www.elsevier.com/locate/gca

# Post-melting oxidation of highly primitive basalts from the southern Andes

S. Tassara <sup>a,b,c,\*</sup>, M. Reich <sup>a,b</sup>, C. Cannatelli <sup>a,b</sup>, B.A. Konecke <sup>d,e</sup>, D. Kausel <sup>a,b</sup>, D. Morata <sup>a,b</sup>, F. Barra <sup>a,b</sup>, A.C. Simon <sup>d</sup>, A. Fiege <sup>f</sup>, E. Morgado <sup>g</sup>, M. Leisen <sup>a,b</sup>

f Department of Earth and Planetary Sciences, American Museum of Natural History, New York 10024-5192, USA

g Institute of Geophysics and Tectonics, School of Earth and Environment, University of Leeds, UK

Received 5 July 2019; accepted in revised form 20 January 2020; Available online 29 January 2020

#### Abstract

The oxygen fugacity (fO<sub>2</sub>) of the Earth's upper mantle and its melting products is an important parameter in the geochemical evolution of arc magmas and their connection with the continental crustal construction and growth. Several works have focused on the  $fO_2$  of peridotite xenoliths, primitive melts in relatively young arc settings, and mid-ocean ridge basalts (MORB) but few studies have attempted to examine the early redox history of primitive magmas in mature arcs. Hence, our understanding of the nature and evolution of fO2 during the subduction cycle remains limited. Here, we investigate the basaltic tephra from the Los Hornitos monogenetic cones in central-southern Chile, which are among the most primitive materials reported in the Southern Andes (olivine Mg#  $\leq$  92.5, and Ni  $\leq$  5000 µg·g<sup>-1</sup>). These features offer a unique opportunity to explore the fO<sub>2</sub> conditions below the Andean arc by studying olivine phenocrysts and their contained crystal and melt inclusions. We integrated EPMA, LA-ICP-MS, and μ-XANES analyses to constrain the redox conditions recorded in the basaltic tephra by three different and self-reliant methods. First, we determined the  $fO_2$  based on the olivine-spinel equilibrium, yielding average values  $\Delta FMQ + 1.3 \pm 0.4$  (1 $\sigma$ ). Second, we constrained the  $fO_2$  conditions of melt inclusions using Fe μ-XANES data and the redox dependent olivine-melt vanadium partitioning. After correcting for post-entrapment crystallization and diffusive iron loss, the Fe  $\mu$ -XANES data indicate that the melt inclusions were trapped in average at  $\Delta$ FMQ  $\pm 2.5 \pm 0.5$  (1 $\sigma$ ). Results using the olivine-melt vanadium partitioning oxybarometer in melt inclusions are in agreement with Fe μ-XANES data, yielding average  $\Delta$ FMQ values of  $+2.6 \pm 0.3$  (1 $\sigma$ ). In order to test the potential effects of other postentrapment modifications of the melt inclusions that could have affected the  $fO_2$  prior to eruption, we assessed the residence time of these magmas using Mg-Fe interdiffusion modelling in olivine. The short residence times (<200 days) compared to vanadium re-equilibration models strongly suggest that the melt inclusions preserve the prevailing fO<sub>2</sub> conditions during their entrapment. Correlations between melt inclusions major element composition and their fO2 determined by Fe µ-XANES, as well as V/Sc modelling reveal a case of post-melting oxidation of the LHC magmas. We argue that primitive arc magmas

E-mail address: tassara.carlos.sant@ug.uchile.cl (S. Tassara).

<sup>&</sup>lt;sup>a</sup> Department of Geology and Andean Geothermal Center of Excellence (CEGA), FCFM, Universidad de Chile, Plaza Ercilla 803, Santiago, Chile

b Millennium Nucleus for Metal Tracing Along Subduction, FCFM, Universidad de Chile, Plaza Ercilla 803, Santiago, Chile
c Department of Geology and Geophysics, Yale University, PO Box 208109, New Haven, CT 06520-8109, USA
d Department of Earth and Environmental Sciences, University of Michigan, Ann Arbor, MI 48109, USA
c ARES, NASA Johnson Space Center, Houston, TX 77058, USA

<sup>\*</sup> Corresponding autor at: Departamento de Geología, Facultad de Ciencias Físicas y Matemáticas, Universidad de Chile, Plaza Ercilla #803, Santiago de Chile, Chile.

behave as an open system with respect to  $fO_2$  during their early geochemical evolution. Our data indicate a complex  $fO_2$  early history of primitive melts in the southern Andes and provide a cautionary note on the direct extrapolation of primitive melts  $fO_2$  values to that of their mantle source.

© 2020 Elsevier Ltd. All rights reserved.

Keywords: Melt inclusions; Arc basalts; Redox; Oxygen fugacity; XANES

#### 1. INTRODUCTION

Direct samples of the deepest portions of the Earth's lithosphere beneath magmatic arcs are provided by either peridotite xenoliths brought to the surface by rapidly ascending magmas, or tectonically exposed crustal sections (Kohistan, Talkeetna, Sierra Nevada, Famatinian arcs) (e.g., Ducea et al., 2015; Jagoutz and Kelemen, 2015; Bucholz and Kelemen, 2019). However, the distribution of these rocks is limited in space and time, hampering our understanding on the nature of the early stages of magmatism. Conversely, olivine-hosted melt inclusions (MIs) constitute a ubiquitous window to investigate deep magmatic processes. Thus, MIs have received increasing attention for tracing the early geochemical history of primitive magmatic systems (Lowenstern, 1995; Sobolev and Chaussidon, 1996; Shimizu, 1998; Laubier et al., 2007; Kent, 2008; Manzini et al., 2017; Reinhard et al., 2018; Søager et al., 2018; Neave et al., 2018; Bouvier et al., 2019; Howarth and Büttner 2019; Hanyu et al., 2019).

Recently, olivine-hosted MIs have also been used to explore the oxygen fugacity (fO2) of their mantle source region, and to evaluate the subsequent post-melting redox history of magmas during storage, differentiation, and ascent (e.g., Kelley and Cottrell, 2012; Hartley et al., 2017; Head et al., 2018). This is of key interest to better constrain, for instance, the fO<sub>2</sub> conditions at which magmas are sourced in the mantle wedge of subduction zones. The predominant view holds that the mantle source region in subduction zones is oxidized due to the reaction with oxidizing fluids derived from the dehydrating slab (Brandon and Draper, 1996; Wood et al., 1990; Parkinson and Arculus, 1999; Kelley and Cottrell, 2009, 2012; Nekrylov et al., 2018). An alternative hypothesis proposes that the  $fO_2$  of the mantle source region in subduction zones is undistinguishable from that of mid-ocean ridges, suggesting that arc basalts inherit their oxidized nature during differentiation on their migration to the surface (Lee et al., 2005, 2010; Dauphas et al., 2009; Mallmann and O'Neill, 2009; Tang et al., 2018). Partial crystallization, assimilation, and degassing can have either an oxidative or reducing effect on ascending magmas depending on the nature of the crystallized or assimilated materials and on the speciation of degassing species (Kelley and Cottrell, 2012; Moussallam et al., 2014, 2016; Gaillard et al., 2015). Recent studies of olivine-hosted MIs have traced evidence of progressive reduction along with differentiation (Kelley and Cottrell, 2012; Hartley et al., 2017). More recently, Tollan and Hermann (2019) showed evidence for continued oxidation of hydrous primitive magmas due to reactions with the surrounding mantle during ascent. This evidence highlights that both source melting and post-melting redox processes that control the  $fO_2$  signature of arc magmas remain enigmatic and require further investigation.

Iron (Fe) is the most abundant redox-sensitive element in magmatic systems and its oxidation state reflects the  $fO_2$  of the system. Thus, the measurement of the oxidized to reduced ratio of Fe, or Fe<sup>3+</sup>/Fe<sup>2+</sup> can be related to the fO<sub>2</sub> of magmas at a given composition, temperature, and pressure (Kress and Carmichael, 1991; Condie, 1993; Hofmann, 1988; O'Connor, 1965; Wilke et al., 2004; Kelley and Cottrell, 2009). Microscale X-ray absorption near edge structure (μ-XANES) spectroscopy allows determination of the speciation of Fe in small-sized samples such as MIs. The Fe<sup>3+</sup>/Fe<sub>tot</sub> ratio of glasses has been calibrated for a range of compositions and fO<sub>2</sub> (e.g., Berry et al., 2003; Cottrell et al., 2009; Farges et al., 2004; Galoisy et al., 2001; Giuli et al., 2003, 2011, 2012; Knipping et al., 2015; Wilke et al., 2004; Fiege et al., 2017), making the use of Fe μ-XANES particularly useful for tracing the early redox processes in MIs. However, the premise that olivine-hosted MIs behave as closed systems after their entrapment (e.g., Sobolev, 1996; Cherniak, 2010) has been challenged by several studies. Both natural and experimental studies have shown that the MI-host system is open to, at least, postentrapment diffusion of Fe<sup>2+</sup> and H<sup>+</sup>. Although H<sup>+</sup> diffusion and fO<sub>2</sub> re-equilibration might occur as independent processes, Fe<sup>2+</sup> diffusion in or out of the MI will have a direct effect on their redox state (Danyushevsky et al., 2000, 2002; Gaetani et al., 2012; Bucholz et al., 2013; Hartley et al., 2015). Therefore, recognizing the extent to which post-entrapment processes affect the  $fO_2$  of a melt inclusion assemblage has become crucial before using them as tracers of deep redox processes. A second approach to constrain the fO2 in olivine-hosted MIs is the redoxdependent partitioning of the multivalent element vanadium (V) between olivine and hydrous basaltic melts (Gaetani and Grove, 1997; Canil and Fedortchouk, 2001; Papike et al., 2013; Laubier et al., 2014; Shishkina et al., 2018). This approach is more robust to post-entrapment modifications because of the trace abundance of V in melts and its generally incompatible behavior in olivine (Shishkina et al., 2018). Therefore, a comparison between various methods to determine fO2, including mineral equilibria (e.g., olivine-spinel equilibrium) and melt inclusionbased oxybarometers may offer a unique opportunity to improve our knowledge about the fO<sub>2</sub> conditions of parental melts, and also test the effects of post-entrapment modifications. Such an approach would be particularly relevant to test in a mature arc setting, where redox data of primitive melts are scarce and the nature and evolution of  $fO_2$  during the subduction cycle remains largely unconstrained.

In this study, we explore the redox record of the primitive basaltic eruptive products of the Los Hornitos mafic monogenetic vents from the transitional Southern Volcanic Zone in the Andes of south-central Chile. These are among the most primitive materials reported in the Southern Andes, with olivine Mg# of up to ∼93 (e.g., Salas et al., 2017). We integrate EPMA, LA-ICP-MS, and Fe μ-XANES analyses of olivine and their contained crystal and MIs to determine their fO<sub>2</sub> values by using a combination of three different and independent oxybarometers, namely olivine-spinel equilibrium, the ratio of oxidized to reduced iron in MIs, and the olivine-melt V partition coefficient. After a detailed assessment of post-entrapment modifications of the MIs and olivine Fe-Mg diffusivity modelling aimed at determining residence times of magmas, our data indicate that despite their primitive nature, the redox evolution of the primitive basaltic magmas of Los Hornitos is more complex than expected. We discuss the possible source and post-melting redox processes that could have caused such fO2 variations and explore their implications for the use of primitive basalts to directly trace their mantle source  $fO_2$  conditions.

# 2. GEOLOGICAL BACKGROUND AND SAMPLE MATERIAL

The Southern Volcanic Zone (SVZ) is a ~1400 km long arc segment that limits with the flat-slab subduction segment to the north at  $\sim 32^{\circ}$ S, and with the subduction of the Chile Ridge to the south at  $\sim 46^{\circ}$ S (Appendix 1). The volcanism of the SVZ is caused by the subduction of the Nazca Plate (convergence velocity of 7 cm/year) beneath the South American continent (DeMets et al., 2010). This segment can be divided into four sub-zones (northern, transitional, central, and southern) based on the geochemistry of the erupted volcanic products, although their precise limits remain uncertain (Sellés et al., 2004; Volker et al., 2011). Within this segment, the volume of primitive basaltic material decreases significantly towards the Northern SVZ because of an increase in the crustal thickness (Tassara and Echaurren, 2012). However, in the Transitional SVZ (TSVZ) there are still a few examples of monogenetic eruptions containing primitive basalts (Salas et al., 2017). Among these, the Los Hornitos Cones (LHC) comprise two small monogenetic vents located ~9 km south of the Cerro Azul/Quizapu stratovolcano, in the Descabezado Grande Volcanic Field (DGVF), within the Chilean TSVZ (35°43'40"S, 70°48'18"W; Appendix 1). The eruptive products of the LHC are basaltic lava flows and pyroclastic material. The tephra material is particularly primitive as evidenced by their olivine Mg# (Mg# = [Mg/(Mg+ Fe) × 100] in molar proportions) reaching values of up to  $\sim$ 93 (Salas et al., 2017).

Melt inclusion studies of eruptive products from the SVZ lavas are scarce and have mostly focused on individual stratovolcanoes (e.g., Witter et al., 2004; Zajacz and Halter, 2009; Rea et al., 2009; Watt et al., 2013). For example, data obtained from olivine-hosted MIs were used predominantly to constrain primitive magma compositions and melt generation parameters (e.g., Weller and Stern, 2018). Wehrmann

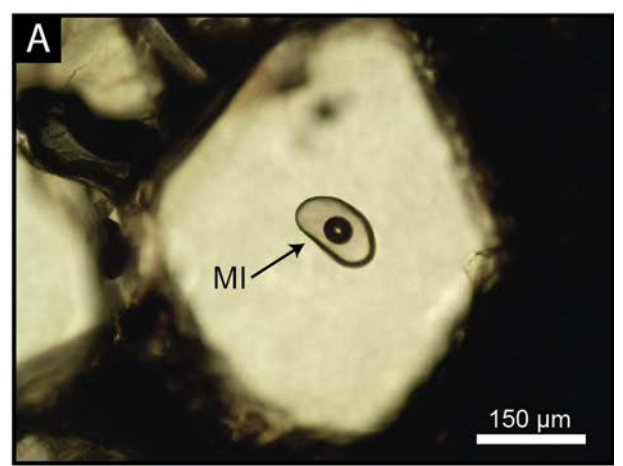
et al. (2014), on the other hand, presented a more regional study that aimed to determine the along-strike variability of volatiles in parental melts in the SVZ. These authors included in their regional analysis melt inclusions data from the LHC, indicating a strong subduction component. Their comparative analyses indicated that the olivine-hosted MIs from the LHC are among the most primitive compositions of the SVZ and suffered sulfur and chlorine outgassing. However, it is important to stress that there are no studies that report  $fO_2$  determinations in MIs of primitive eruptive materials in the SVZ, hampering our understanding of processes that occur in the mantle source of the parental melts.

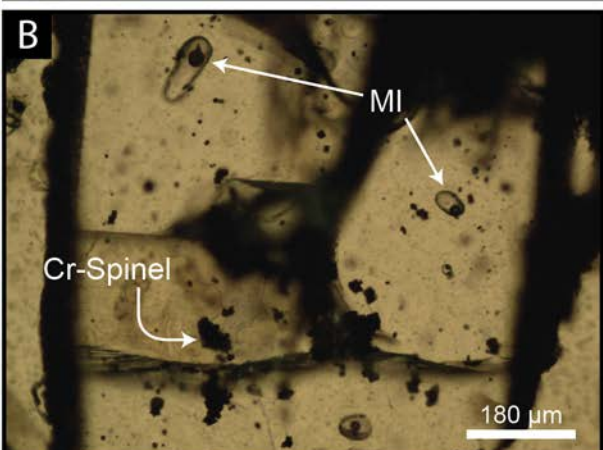
In this study, we focus on the basaltic tephra from the explosive stages of the LHC because olivine-hosted inclusions in this material are less susceptible to recrystallization than in basaltic lavas (Lloyd et al., 2013; Hartley et al., 2017). The tephra material is rich in euhedral olivine phenocrysts that contain abundant Cr-spinel and melt inclusions. Olivine grains were hand-picked and inspected individually for the occurrence of MIs. Detailed petrographic observations revealed that MIs are present in almost all olivine grains from the LHC. The inclusions are colorless to light brown, rounded to elongated and vary in size from 10 to 90 µm (Fig. 1A-C). Except for the smallest MIs ( $\sim$ 5–10 µm), they always display a shrinkage bubble and commonly, accidental crystals of Cr-spinel (crystals arbitrary enclosed during the entrapment of melt inclusions). These features are characteristic of olivinehosted MIs reported in the literature (Cannatelli et al., 2016, and references therein). The MIs commonly occur as isolated inclusions, making it difficult to define genetically linked melt inclusion assemblages (MIA) genetically related due to the lack of symmetry in olivine. For analysis, the olivine phenocrysts were mounted in epoxy mounts and polished individually until MIs were exposed. MIs were carefully examined and selected to avoid cracks and embayments that could have reset the system after the melt entrapment. In addition, only MIs completely enclosed within the host crystal and devoid of any evidence of recrystallization were picked for analysis.

# 3. ANALYTICAL METHODS

# 3.1. Electron probe microanalysis (EPMA) and electron backscatter diffraction (EBSD)

The concentrations of major and minor elements in olivine, Cr-spinel, and MIs were quantitatively characterized by wavelength-dispersive spectrometry (WDS) using a CAMECA SX-100 electron microprobe in the Electron Microbeam Analysis Lab (EMAL) at the University of Michigan, USA. An acceleration voltage of 20 kV, a beam current of 10 nA, and a focused (1  $\mu$ m) beam were used for olivine and Cr-spinel analyses. Counting times of 20 s on the peak and 10 s on the background position were used for all elements. For melt inclusion analysis, an acceleration voltage of 15 kV, a beam current of 5–10 nA, and a beam size of 5  $\mu$ m was used. A peak counting time of 10 s was used for all elements when analyzing the MIs, except for Na and K where 5 s was used. Precautions were taken to





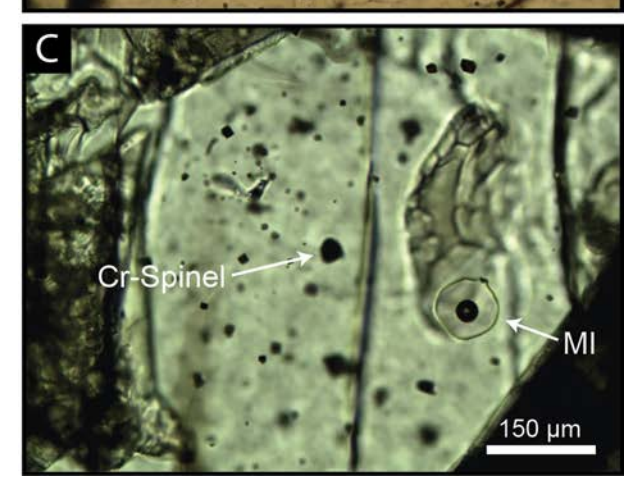


Fig. 1. Plane polarized light images of olivine-hosted MIs from the LHC basaltic tephra. (A) MIs selected for study are commonly located in the center of olivine phenocrysts and far from any fracture and/or embayment, and devoid of any signs of recrystallization. (B) and (C) show typical occurrences of MIs, along with tens of Cr-spinel crystals within the same olivine host.

prevent electron beam damage of glass (e.g., alkali and Si diffusion, and Al burn-in; Morgan and London 2005). Analyses were spotted away from fractures or defects. Olivine-MI and olivine-spinel pairs were analyzed between 25 and 30 μm away from other phases, fractures or defects. Whereas olivine was analyzed twice and averaged when

possible, Cr-spinel were analyzed once in the center of the crystal as they were just too small to probe different locations.

Crystallographic orientations of olivine crystals were determined using electron back-scatter diffraction methods (EBSD; Prior et al., 1999). These data were used in diffusion modelling, considering the fact the Fe-Mg diffusivity depends on the crystallographic orientation of olivine crystals (Dohmen and Chakraborty, 2007; Dohmen et al., 2007). The EBSD data were obtained using a FEI Quanta 650 field emission scanning electron microscope (FE-SEM) equipped with a Nordlys EBSD camera at the School of Earth and Environment, University of Leeds, UK.

# 3.2. Micro X-ray absorption near edge structure spectroscopy $(\mu\text{-XANES})$

In situ u-XANES analyses at the Fe K-edge were performed at the GSECARS 13-ID-E beamline of the Advanced Photon Source (APS), Argonne National Laboratory (Illinois, USA). The beamline covers an energy range of 2.4–28 keV and uses a set of Kirkpatrick-Baez (KB) focusing mirrors that result in a  $2 \mu m \times 2 \mu m (\mu$ -XANES) focused beam, allowing for high spatial resolution. Energy selection was achieved using a Si (111) channel cut monochromator. The energy of the first derivative peak of Fe metal foil was set to the F K-edge energy of 7110.75 eV as determined by Kraft et al. (1996). All spectra were collected in fluorescence mode from 7062 to 7308 eV with a counting time per point of 1 s and step sizes of 3 eV from 7062 to 7107 eV; 0.1 eV from 7107 to 7137 (pre-edge): 2 eV from 7137 to 7308 eV. We emphasize that the fluorescence mode was chosen due to the nature of the samples which did not allow for transmission mode. All u-XANES data were corrected for detector dead time and self-absorption. The XANES spectra were processed and calibrated according to the method described by Fiege et al. (2017).

# 3.3. Laser ablation inductively coupled plasma mass spectrometry (LA-ICP-MS)

The concentration of trace elements (La, Ce, Nd, Sm, Eu, Gd, Dy, Ho, Er, Yb, Lu, Rb, Ba, Th, U, Sr, Zr, Hf, Ti, Ni, and V) in olivine and MIs were obtained by laser ablation inductively coupled plasma mass spectrometry (LA-ICP-MS), using a ArF excimer laser 193 nm (Photon Machines Analyte G2) coupled to a quadrupole ICP-MS (ThermoFisher Scientific iCAPQ) at the Mass Spectrometry Laboratory of the Andean Geothermal Center of Excellence (CEGA), Universidad de Chile, Santiago. The counting time for one analysis was typically 180 s (60 s on gas blank to establish background and 120 s for data collection), unless limited by the small volume of material for the case of the MIs. The diameter of the laser beam was 12–40 μm, the frequency 7 Hz, and 4 J/cm<sup>2</sup> of laser fluence. A maximum of 15 unknowns were bracketed by the measurement of two external standards: the NIST SRM 610 (primary) and the USGS BHVO2G (secondary). The secondary standard was repetitively analyzed and treated as

an unknown, yielding both precision and the accuracy better than 10% for the analytical session. The data reduction was carried out using the Iolite software (Woodhead et al., 2007; Paton et al., 2011); Si or Al contents—determined by EMPA — were used as internal standards. Detection limits and standard errors for each element are presented in Appendix 2.

#### 3.4. Oxygen fugacity determination

We assessed the fO<sub>2</sub> values of the basaltic tephra material from LHC by using three different and independent methods. The first one involves the olivine-spinel equilibrium, which is one of the most common approaches to estimate the redox state of upper mantle and basaltic rocks. The foundation of this oxybarometer relies on the presence of both Fe<sup>2+</sup> and Fe<sup>3+</sup> in spinel (Irvine, 1965), and several models have been developed (O'Neill and Wall, 1987; Mattioli and Wood, 1988; Ballhaus et al., 1991). We used the model of Ballhaus et al. (1991) (and its associated erratum; Ballhaus et al., 1994), based on the olivineorthopyroxene-spinel equilibrium, to constrain the fO<sub>2</sub> of the melts that produced the tephra material from LHC. This model is also applicable to orthopyroxeneundersaturated systems, at the risk of increasing the uncertainty in up to  $\sim 0.2$  log units, as long as  $X_{Fe}^{ol} < 0.15$ (Ballhaus et al., 1991). Temperature was calculated using the Fe-Mg spinel-olivine equilibrium thermometer (Ballhaus et al., 1991), and pressure was assumed to be 1 GPa, resembling crustal pressures estimated for the TSVC (Tassara and Echaurren, 2012). Variations of 1 GPa in pressure would result in  $\sim 0.23$  log units difference in  $fO_2$ . The second oxybarometer takes into account the oxidation state of Fe (Fe<sup> $^{^{2}+}$ </sup> vs. Fe<sup> $^{3+}$ </sup>) in the MIs to determine  $fO_2$ . The Fe<sup>3+</sup>/Fe<sub>tot</sub> ratios of the studied MIs were obtained using Fe μ-XANES following the procedure of Fiege et al. (2017), and the fO<sub>2</sub> values were translated to log units with respect to the FMQ buffer using Eq. 7 of Kress and Carmichael (1991), at 1200 °C and 1 GPa. The third approach involves olivine-melt redox dependent vanadium (V) partitioning. Vanadium can be present as +2, +3, +4, and +5, although valences +3 and +4 prevail in natural magmatic systems (Borisov et al., 1987; Sutton et al., 2005). In Fe-Mg silicates,  $V^{4+}$  is more incompatible compared to  $V^{3+}$ . Therefore, rising  $fO_2$  will increase the  $V^{4+}/V^{3+}$  ratio of the melt, modifying the partition coefficient of V between the silicates and the melt. We used the calibration of Shishkina et al. (2018) to determine the  $fO_2$  in the MIs based on their V content measured using LA-ICP-MS. This method is based on the fO<sub>2</sub>-dependent partitioning of V between olivine and melt  $D_{v}^{ol/melt}$ ) and was calibrated at temperatures between 1025 and 1150 °C, and pressures between from 0.1 to 0.3 GPa (Shishkina et al., 2018).

#### 4. RESULTS

# 4.1. Olivine composition

Olivine was the only significant phenocryst recovered from the tephra material at LHC. The olivine phenocrysts

are colorless to greenish-colored, euhedral to subhedral, and vary in size from  $\sim$ 150 to 1500  $\mu$ m (Fig. 1A and B). Excluding a few smaller crystals (<200 µm), olivine phenocrysts always host tens of µm-sized Cr-spinel mineral inclusions. The composition of the olivine cores hosting the Cr-spinel inclusions vary from 46.6 to 52.5 wt% MgO (Mg# from 87.6 to 92.5, with an average value of 91.1; Appendix 2). Selected in-situ trace element data of olivine obtained by LA-ICP-MS are presented in Appendix 2. Nickel concentrations range from 1360 to 5190 µg·g<sup>-1</sup> and correlate positively with Mg# values. The most primitive olivine crystals have Ni contents slightly higher than those expected from simple melting of a peridotite source at a given Mg# (Herzberg, 2011), although they follow a typically low Ni fractionation trend (Appendix 2). The CaO concentration was determined by EPMA due to <sup>40</sup>Ca interference with <sup>40</sup>Ar during LA-ICP-MS analysis, and is slightly lower (1100-1700 µg.g<sup>-1</sup>) than expected for olivine crystallized from peridotite-derived melts (0.2-0.3 wt.%, 10) (Sobolev et al., 2007; Gavrilenko et al., 2016). The Fe/Mn ratios range between 41.8 and 58.9 (Appendix 2) and are also consistently lower than olivine derived from peridotite melts (Sobolev et al., 2007). The Cr content (148-590 μg·g<sup>-1</sup>) correlates positively with Ni ( $R^2 = 0.64$ ) and Al  $(R^2 = 0.5)$ . The Al concentration of olivine  $(72-202 \,\mu\text{g}\cdot\text{g}^{-1})$ correlates positively with Ni ( $R^2 = 0.47$ ) and negatively with Mn ( $R^2 = 0.33$ ) (Appendix 2).

#### 4.2. Cr-spinel composition

Cr-spinel inclusions occur as reddish to dark-brown euhedral crystals, ranging in size from 3 to 10 µm, commonly forming clusters of up to 10 crystals within olivine (Fig. 1B and C). Although the spinel inclusions are small, the low SiO<sub>2</sub> content measured (<0.15 wt.%) suggests that there is no significant secondary fluorescence affecting the spinel measurements (details in Appendix 3). Twenty-one Cr-spinel inclusions were analyzed in different olivine crystals, as well as the respective olivine hosts (Appendix 3). The Cr-spinel inclusions show a narrow compositional range with Cr# varying from 63.5 to 74.1 (Cr# = [Cr/(Cr + Al)  $\times$  100] in molar proportions). These Cr# values are similar to Cr-spinels with the highest Cr# reported in the literature, underscoring their highly primitive nature (e.g., Kamchatka picrobasalts, Cr# = 60-80, Portnyagin et al., 2005; Nekrylov et al., 2018). The Mg# of the Cr-spinel inclusions varies from 40.4 to 60.3 mol.%, even within the narrow range of Mg# content of the host olivine (Appendix 3). The Cr# of the spinel correlates negatively with its Fe<sup>3+</sup> contents ( $R^2 = 0.56$ ; Fe<sup>3+</sup> calculated based on perfect stoichiometry and charge balance). There is no clear correlation between the Mg# of the Cr-spinel inclusions and the Mg# of their olivine hosts.

# 4.3. Melt inclusion composition

The major and minor element concentrations of the olivine-hosted MIs (normalized to a water free basis) can be found in Appendix 2. The measured MgO concentration range from 4.5 to 9.8 wt.%, and the SiO<sub>2</sub> concentrations

vary from 46.4 and 54.9 wt.%. The FeOtot and K2O contents are 5.2-9.6 wt.% and 0.4-1.2 wt.%, respectively. Major elements concentration versus the MgO content show no correlation for  $FeO_{tot}$  ( $R^2 = 0.04$ );  $Al_2O_3$  and TiO<sub>2</sub>, on the other hand, show a weak positive correlation with decreasing MgO (R<sup>2</sup> of 0.12 and 0.15, respectively). CaO decreases with increasing  $FeO_{tot}$  ( $R^2 = 0.32$ ) and increases with increasing  $Al_2O_3$  ( $R^2 = 0.51$ ), whereas alkalis also show a weakly positive correspondence with increasing  $Al_2O_3$  ( $R^2 = 0.14$ ). The non-normalized total oxide wt.% of the analyzed MIs range from 94 to 99.78, likely due to the presence of significant amounts of water (Wehrmann et al., 2014; Salas et al., 2017). Sulfur concentrations are widely variable, ranging from  $\sim$ 550 to  $\sim$ 3740 µg.g<sup>-1</sup>, and Cl varies between 770 and  $2278 \, \mu g \cdot g^{-1}$  (average  $1\sigma$ : 30 and  $25 \,\mu \text{g} \cdot \text{g}^{-1}$ , respectively), as commonly reported in arc magmas (Wallace 2005; Straub and Layne 2003). Chlorine concentrations show a weak positive correlation with sulfur  $(R^2 = 0.32)$ . Post-entrapment modifications and the recalculated composition of the MIs are addressed and discussed in Section 4.5.

The trace element composition of the MIs is presented in Appendix 2 and their primitive upper mantle (PUM) normalized patterns (McDonough and Sun, 1995) are displayed in Fig. 2. All analyzed inclusions show similar trace element contents and distribution patterns are typical

of arc magmas. They have relatively flat PUM-normalized patterns, particularly for the least incompatible elements, with concentrations lower than the average N-MORB (Fig. 2). The most notorious aspects of the trace element composition are the strongly positive Sr and Pb anomalies, and negative Nb anomalies (Fig. 2), similar to those reported for primitive arc basalts (Schmidt and Jagoutz, 2017). An enrichment in large-ion lithophile elements (LILE, Ba, and Sr) is observed, and shows a good correspondence with K contents. The La/Yb ratios are relatively low and vary between 2.5 and 6.5, whereas the Rb/Yb ratios can be as high as 17.2 (Fig. 2).

When compared to the global composition of primitive arc magmas, the major and trace element signature of the olivine-hosted MIs studied here resembles those of primitive calc-alkaline basalts from intra-oceanic arcs such as from New Zealand, Aleutians, and the Solomon Islands (Sorbadere et al., 2011; Schmidt and Jagoutz, 2017).

### 4.4. Iron µ-XANES analysis of melt inclusions

Iron  $\mu$ -XANES spectra were collected on a total of 45 melt inclusions from among 32 olivine host crystals. Based on the shape of the post-edge region of the acquired spectra, a total of ten spectra that were clearly devoid of olivine host contamination were used to calculate the Fe<sup>3+</sup>/Fe<sub>tot</sub>

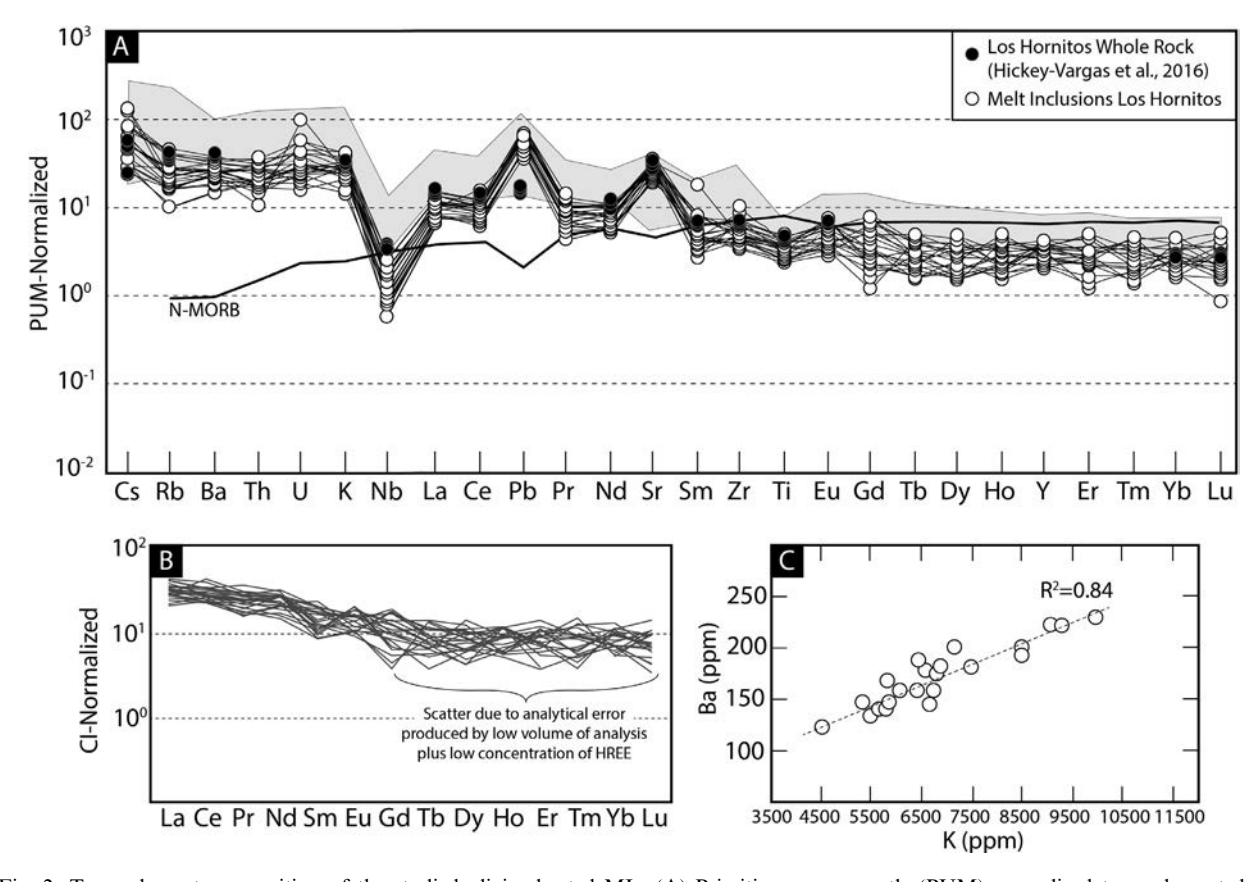


Fig. 2. Trace element composition of the studied olivine-hosted MIs. (A) Primitive upper mantle (PUM)-normalized trace element data obtained by LA-ICP-MS. Bulk rock geochemical data of the LHC and volcanic products of the Descabezado Grande Volcanic Field are shown for comparison (shaded field; Hickey-Vargas et al., 2016). N-MORB field after McDonough and Sun (1995). (B) Rare earth element (REE) data of olivine-hosted MIs determined by LA-ICP-MS methods. (C) Melt inclusion Ba vs. K bivariant plot, showing a typical of arc magmas signature influenced by a slab fluid component.

ratio of the melt inclusion (Fig. 3). Although the Fe<sup>3+</sup>/Fe<sub>tot</sub> ratio can be slightly affected by melt composition and temperature (Kress and Carmichael 1991; Moretti, 2005), Fiege et al. (2017) have recently provided empirical calibrations for basaltic glasses that allow for the accurate determination of fO<sub>2</sub> from the Fe<sup>3+</sup>/Fe<sub>tot</sub> data obtained at the GSE-CARS 13-ID-E beamline of the Advanced Photon Source (APS). The calculated centroid energy of the pre-edge (Fig. 3) has been shown to be a function of the Fe<sup>2+</sup> and Fe<sup>3+</sup> relative contributions, where the weighted centroid changes gradually from Fe<sup>2+</sup>- to Fe<sup>3+</sup>-dominated with increasing oxidation state of felsic to basaltic melts (e.g., Berry et al., 2003; Cottrell et al., 2009; Fiege et al., 2017). We used the recently described methods of Fiege et al. (2017) to fit and calibrate the measured spectra. The Fitvk software (Wojdyr 2010) was used to fit the background spectra through a combination of exponentially modified Gaussian and linear functions and, subsequently, adding Gaussian functions to fit the background-corrected preedge peak. Fityk provides the intensity peak and area of each Gaussian, which were used to calculate the centroid energy position. We used the basaltic glass data of Fiege et al. (2017) as check standards for the data processing and calculation of the Fe3+/Fetot ratios, leading to identical results within error. The measured Fe<sup>3+</sup>/Fe<sub>tot</sub> ratios of the studied MIs range from 0.37 to 0.49 (average 0.437  $\pm$  0.05, 1 $\sigma$ ) (Appendix 2). We acknowledge that the high fluxes used in the 13-ID-E GSCARS beamline at the APS might result in oxidation during beam irradiation and

spectra acquisition (Cottrell et al., 2018). Recommended precautions to avoid this effect include defocusing the beam spot and/or attenuating the beam. However, whereas these corrections result in lower photon fluxes potentially preventing beam damage, defocusing the beam (increasing spot size) resulted in significant contamination of the spectra with surrounding olivine host (Fig. 3; upper spectrum), making it impossible to acquire MIs data at the recommended photon flux values ( $<3 \times 10^6$  photons/s/ $\mu$ m<sup>2</sup>). Still, attenuation of the photon flux was possible through the use of an aluminum foil. A rough estimation of the photon flux density used during the analyses reported in this study is  $\sim 5 \times 10^9$  photons/s/ $\mu$ m<sup>2</sup>. Despite these potential inconveniences, it is important to note that our Fe μ-XANES results are in excellent agreement with the olivine-melt vanadium partitioning data, indicating that our data were not (or were minimally) affected beyond error (see Section 3.6 for details). The effects of post-entrapment modifications on the Fe3+/Fetot ratios of the MIs are discussed below.

## 4.5. Post-entrapment modification of melt inclusions

The assumption that MIs behave as closed systems after their entrapment in a crystal host renders its potential to trace the composition of near-primary melts in volcanic systems (Sobolev, 1996; Cherniak, 2010). However, several studies have highlighted that post-entrapment processes can significantly modify the original composition of the

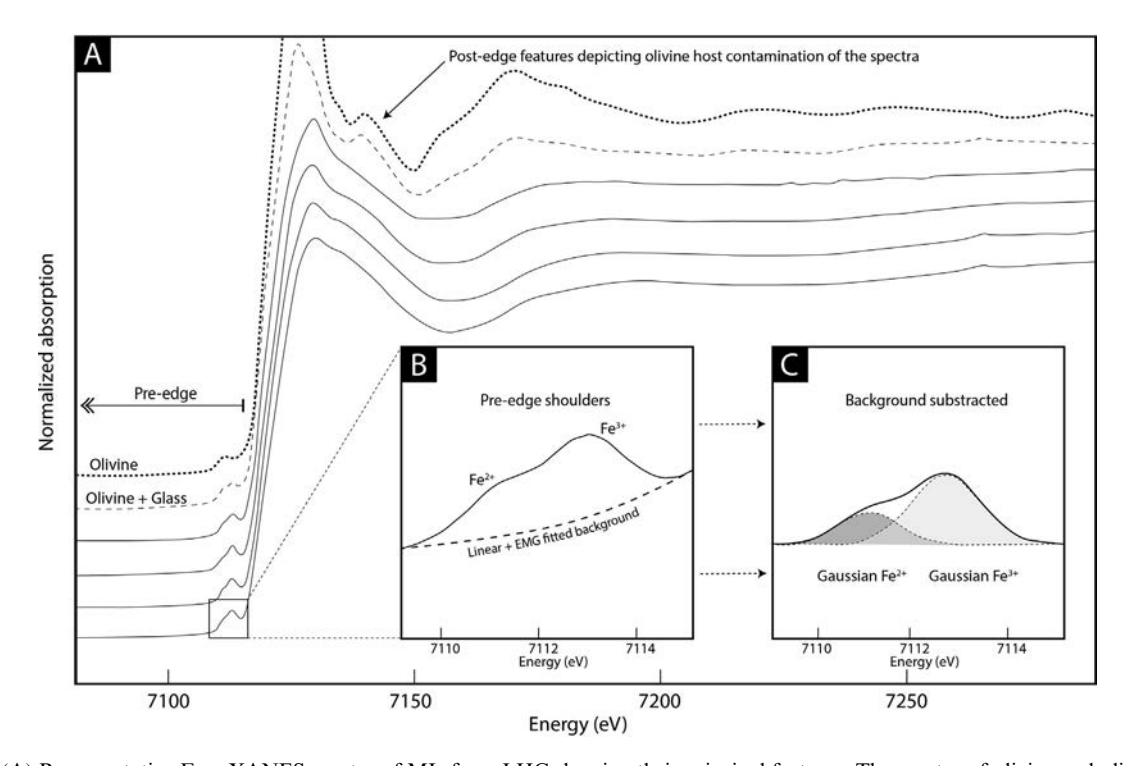


Fig. 3. (A) Representative Fe  $\mu$ -XANES spectra of MIs from LHC showing their principal features. The spectra of olivine and olivine-melt inclusion mixture is also shown to underline the importance of checking the quality of the spectra. Host-contaminated melt inclusion spectra display post-edge features typical of olivine. (B) and (C) illustrate the fitting procedure where the fitted background is subtracted from the preedge region of the spectra (B). The position of the centroid energy is calculated afterwards based on the area and peak center of each of the gaussians applied to the Fe<sup>2+</sup> and Fe<sup>3+</sup> shoulders, respectively (C).

Gurenko et al., 1991; Sovolev (e.g., Danyushevsky, 1994; Danyushevsky et al., 2000, 2002). In the particular case of olivine-hosted MIs, post-entrapment crystallization (PEC) is a near ubiquitous process altering the composition of the originally trapped melt (Hartley et al., 2017). During cooling of the melt inclusion-olivine system, olivine can crystallize at expense of the melt in the inclusion and form a rim along the inclusion wall, lowering the Mg# of the theoretical olivine in equilibrium with the remaining melt, and resulting in disequilibrium with the olivine host (Fig. 4). In addition to PEC, post-entrapment modifications reported in olivine hosted MIs include both hydration and dehydration (Portnyagin et al., 2008; Chen et al., 2011; Gaetani et al., 2012; Hartley et al., 2015), loss of volatiles such as CO<sub>2</sub> (Anderson and Brown, 1993; Mironov and Portnyagin, 2011; Bucholz et al., 2013), as well as diffusive loss of SiO<sub>2</sub> (Portnyagin et al., 2019) and Fe<sup>2+</sup> (Danyushevsky et al., 2000, 2002). In turn, the Mg# gradient within the newly formed rim of olivine after PEC can trigger or enhance Fe<sup>2+</sup> loss (Danyushevsky et al., 2000, 2002). This process involves diffusive loss of Fe from the inclusion and gain of Mg, leading to a decrease in the total Fe content (Danyushevsky et al., 2000) (Fig. 4). Given the highly incompatible behavior of Fe<sup>3+</sup> in olivine, both PEC and Fe<sup>2+</sup> loss will increase the Fe<sup>3+</sup>/Fe<sub>tot</sub> ratio of the inclusion, significantly altering the original fO2 of the trapped melt. Thus, assessing the extent to which this process occurred is fundamental before addressing the valence of Fe in olivine-hosted MIs.

The MIs studied here are clearly in disequilibrium with their olivine host, as the Mg# of the olivine in equilibrium with the melt is significantly lower than our measured values for the host (Appendix 2). Fig. 5A and 5B shows that

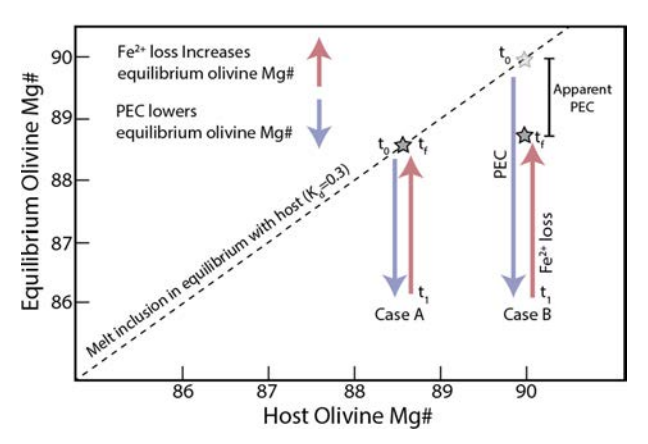


Fig. 4. Comparison of the Mg# of olivine in equilibrium with the melt inclusion (see BSE image in Fig. 5A) against the Mg# of the olivine host. The diagram shows the different effects of postentrapment crystallization (PEC) and post-entrapment  $Fe^{2+}$  loss on the Mg# of olivine. PEC will reduce the Mg# of equilibrium olivine, plotting below the equilibrium ( $K_{\rm d}=0.3$ ; dashed line). In contrast,  $Fe^{2+}$  loss will lead to increase the Mg# of equilibrium olivine. Case A illustrates the scenario where significant  $Fe^{2+}$  loss occurred after PEC, resulting in a melt inclusion in equilibrium with its olivine host yet with lower FeO content than the original trapped melt. Case B shows the case where the melt inclusion underwent significant PEC followed by little  $Fe^{2+}$  loss, resulting in a Fe/Mg disequilibrium where Fe-loss could remain unnoticed.

PEC was certainly in part responsible of this disequilibrium. However, correcting for PEC alone does not necessarily result in the composition of the originally trapped melt. For example, as explained by Laubier et al. (2012), if an inclusion is trapped at ~1300 °C and cools to  $\sim$ 1200 °C, PEC will take place. If the system is kept at ~1200 °C for enough time or the system is subject to slow cooling, the Mg# gradient between the melt inclusion and the olivine host will promote further diffusion of Fe out of the inclusion (Danyushevsky et al., 2000). The overall result of the combined processes could result in a melt inclusion with lower FeO concentration, but still in equilibrium with the host (Fig. 4). If olivine continues to grow within the inclusion, then the Mg# of the olivine in equilibrium will decrease. Correcting for PEC using reverse crystallization would thus result in the composition of the low-FeO inclusion in equilibrium with the host, but not that of the originally trapped melt. To identify this effect, we contrasted the size of the MIs to their FeO content. Smaller MIs re-equilibrate with their host faster than bigger melt inclusions (e.g., Qin et al., 1992). Fig. 5C compares the size and FeO content of MIs, depicting that smaller MIs have lower FeO contents ( $R^2 = 0.41$ ). The latter, coupled with the generally lower FeO in MIs compared to the whole rock data (Fig. 5C), is strong evidence that Fe-loss occurred in addition to PEC in the suite of studied melt inclusions.

The lower FeO content of the inclusions caused by Fe<sup>2+</sup> loss has two main effects on its composition: (1) it will increase the relative concentration of all other major elements in the melt inclusion and (2) it will significantly increase its Fe<sup>3+</sup>/Fe<sub>tot</sub> ratio. Whereas (1) is not of great relevance for the purposes of this study, (2) is critical and needs revision. Laubier et al. (2012) corrected the diffusive Fe<sup>2+</sup> loss of olivine-hosted MIs based on correlations between trace elements and FeO contents. However, our trace element data do not show a similar trend, precluding the use of this method. In addition, modelling fractional crystallization of olivine and spinel using our most primitive compositions shows that the expected FeO variation under the range of MgO compositions of the MIs studied here would be close to 0.31 wt.% at the highest. This variation is lower than the analytical error  $(1\sigma)$  for FeO obtained from the microprobe data (average: 0.36 wt.%). Therefore, we adopted the method used by Danyushevsky et al. (2000), which consist of a correction based on eliminating any FeO variations that may have been originally present (i.e., defining a constant FeO content for the inclusions). To perform the PEC and Fe-loss correction we used the Petrolog3 software (Danyushevsky and Plechov, 2011). We used the olivine equilibrium model of Ford et al. (1983) at  $\Delta$ FMQ + 2 and 1 GPa, and Fe<sup>3+</sup> was assumed to be perfectly incompatible within olivine. A total FeO content of 7.62 wt.% of the melt inclusions was used, as defined by the average of whole rock data for the same volcanic products (Salas et al., 2017). Results show that the studied MIs have undergone variable PEC, ranging from 0.3 to 16.48 % by weight. In particular, for the MIs having their Fe<sup>3+</sup>/Fe<sub>tot</sub> measured by µ-XANES we recalculated the original composition of the melt inclusions using both closed and open system behavior of melt inclusions with respect to fO2. All

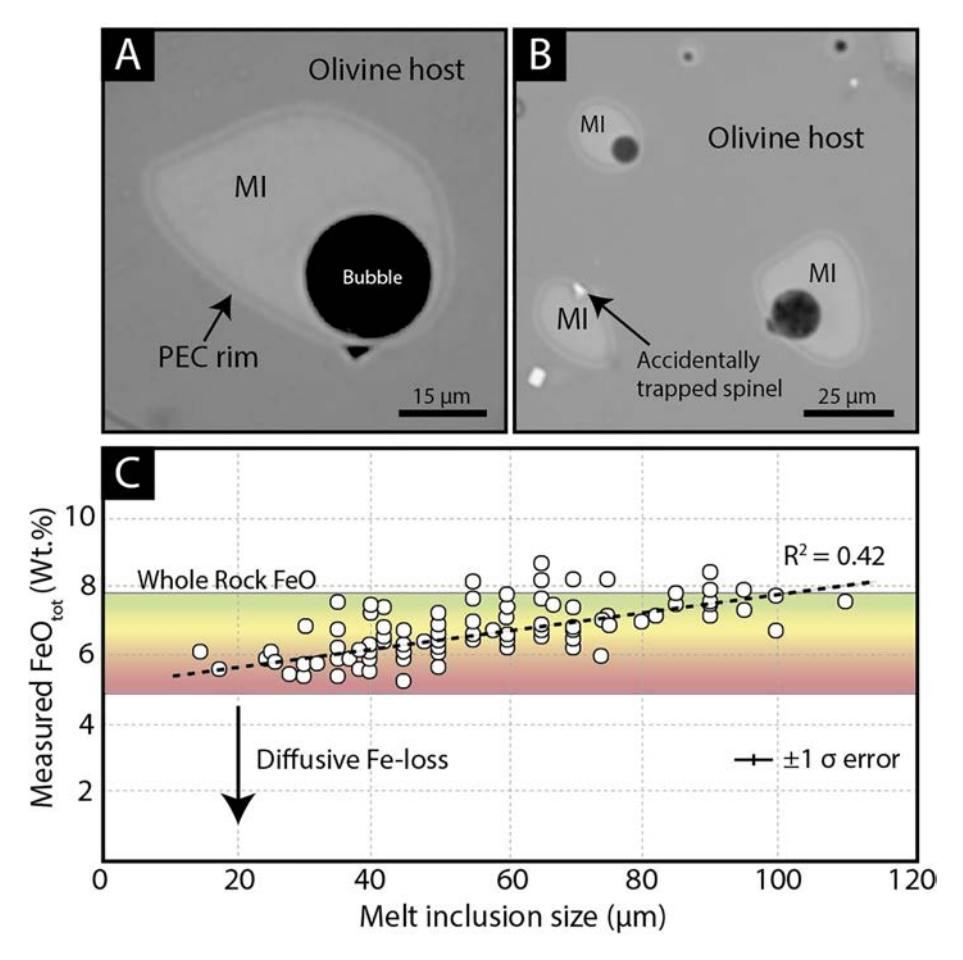


Fig. 5. Backscattered electron (BSE) images of olivine-hosted MIs from the LHC basaltic tephra. (A) Example of a melt inclusion showing a PEC rim of olivine ("equilibrium olivine") around its wall. (B) Melt inclusion assemblage also showing PEC rims, and accidentally trapped Cr-spinel crystals. (C) Measured FeO<sub>tot</sub> (wt.%) of olivine-hosted melt inclusions plotted against their size. Scale of colors represent degrees of diffusive Fe-loss from green (no Fe-loss) to red (severe Fe-loss).

the corrected data are presented in Appendix 2. We discuss the effects of this correction on the original  $Fe^{3+}/Fe_{tot}$  ratios in the next section.

### 4.6. Redox state constraints

The determination of fO2 of the LHC basaltic tephra material using the olivine-spinel equilibrium model of Ballhaus et al. (1991) yields ΔFMQ values between +0.8 and +1.9 (mean +1.3  $\pm$  0.4, 1 $\sigma$ ) (Table 1, Appendix 3). The uncertainties in the  $\Delta$ FMQ values were calculated as the propagated error from the calculations of each of the variables involved in the equation, including the EPMA data, the stoichiometric Fe<sup>3+</sup> content estimated for Crspinel, the equilibrium temperature, plus the SiO<sub>2</sub> activity of the system (Fig. 7). In light of recent studies emphasizing the importance of using standard reference materials for the Fe<sup>3+</sup>/Fe<sub>tot</sub> ratio of spinel (Davis et al., 2017), we notice that the calculation of the Fe<sup>3+</sup> content of the Cr-spinel based on pure stoichiometry and charge balance is not as precise as it could be. Davis et al. (2017) demonstrated that uncorrected measurements of spinel can have Fe3+/Fetot values off by 0.03 from those measured via Mössbauer spectroscopy. To account for this issue, we have added to the propagated uncertainty  $a \pm 0.03$  error in the calculated Fe<sup>3+</sup>/Fe<sub>tot</sub> ratio of the Cr-spinel studied here, which translates into an additional uncertainty of  $\pm \Delta FMQ$  between 0.25 and 0.5, even when considering the error that changes in the Fe<sup>3+</sup>/Fe<sub>tot</sub> ratio of the Cr-spinel impart on the in calculated equilibrium temperature. Furthermore, although Ballhaus et al. (1991) noted that their oxybarometer gave reasonable results for orthopyroxene undersaturated rocks, deviations from the enstatite-forsterite-silica buffer of 0.1 log units in the silica activity translates into a 0.3 log units error in fO<sub>2</sub>. Therefore, we calculated the silica activity of the LHC system based on both whole-rock data (Salas et al., 2017) and averaged melt inclusions composition using the MELTS supplemental calculator. Fig. 6 shows that the data falls close to the enstatite-forsterite-silica Buffer with differences ΔEn-Fo values up to 0.03. Accordingly, an additional error in the  $fO_2$  estimations of 0.1 log units was added to the calculated uncertainty. The calculated propagated uncertainty for each Cr-spinel-olivine pair vary between 0.35 and 0.81 log units, being largest when the  $\Omega_{1-27}$ 

Sp-47

Ol-47

Sp-54

O1-54

Sp-14

Ol-14

Average Std. Dev. (Sp)

Summary of data u	used in the estin	mation o	of $fO_2$ bas	ed on the	e olivine-	spinel e	quilibriun	n.				
Crystal #	MgO	$SiO_2$	$Al_2O_3$	FeO	MnO	NiO	$Cr_2O_3$	CaO	$TiO_2$	Total	T (K)	$\Delta FMQ^*$
Sp-17	12.31	0.10	13.82	24.16	0.37	0.09	45.99	0.03	0.41	97.31	1405	1.66
Ol-17	47.60	41.13	0.001	11.86	0.16	0.17	0.04	0.15	0.00	101.13		
Sp-26	14.16	0.11	13.64	16.71	0.33	0.19	52.82	0.02	0.23	98.24	1415	0.79
Ol-26	49.47	41.42	0.02	9.13	0.14	0.32	0.04	0.15	bdl	100.72		
Sp-32	14.21	0.11	13.61	16.79	0.34	0.19	52.88	0.01	0.24	98.43	1420	0.83
Ol-32	49.54	41.47	0.01	9.12	0.15	0.33	0.04	0.15	bdl	100.85		
Sp-54	14.81	0.09	14.74	18.43	0.32	0.20	48.15	0.01	0.37	97.16	1439	1.80
Ol-54	50.62	40.44	0.04	8.44	0.14	0.39	0.06	0.15	bdl	100.31		
Sp-27	14.32	0.11	13.56	16.81	0.34	0.20	52.50	0.02	0.24	98.12	1435	0.93

0.14

0.34

0.13

0.33

0.11

0.32

0.13

0.02

0.02

0.34

0.19

0.41

0.21

0.39

0.19

0.34

0.02

0.02

0.04

50.41

0.08

47.17

0.07

52.24

0.04

0.20

0.05

0.15

0.01

0.13

0.02

0.15

0.02

0.16

0.01

0.02

bdl

0.30

0.00

0.39

0.02

0.26

bdl

0.02

0.02

100.59

97.18

100.75

97.30

101.22

97.69

100.39

1381

1411

1420

1.55

1.89

0.94

Table 1

49.39

14.21

50.48

14.81

51.03

14.20

49.30

41.49

0.10

41 16

0.09

0.12

41.47

0.02

40.93

0.02

0.01

13.56

15.59

0.03

0.02

0.14

13.50

9.01

18.02

18.67

8.47

16.81

8.91

0.22

8 32

<sup>&</sup>lt;sup>a</sup> The uncertainty represents the errors on the microprobe data, stoichiometric determination of ferric iron in spinel, equilibrium temperature, and silica activity of the system.

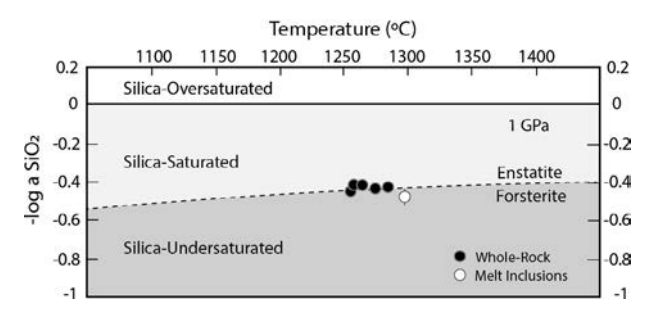
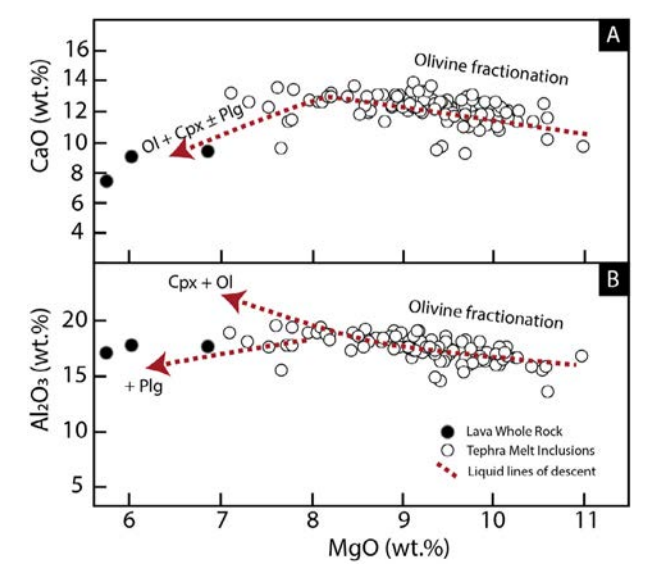


Fig. 6. Silica activity of the LHC basalts compared to the Enstatite-Forsterite buffer at 1 GPa at variable temperatures. The Enstatite-Forsterite buffer was calculated using the MELTS supplemental calculator, which uses thermodynamic data from Berman (1998). Temperatures correspond to the whole-rock liquidus calculated using rhyolite-MELTS (Gualda et al., 2012).

Cr-spinel composition has low ferric iron concentrations, as noticed by Davis et al. (2017) (Table 1; Appendix 3). These data show that the primitive melts from LHC are up to  $\sim 2$ ΔFMQ units more oxidized that mid-ocean ridge basalts (MORBs), which usually record ΔFMQ values between -0.1 and +0.3 (Cottrell and Kelley, 2011; O'Neill et al., 2018; Zhang et al., 2018). The slightly oxidizing conditions recorded in LHC are characteristic of typical arc magmas., i.e.,  $\Delta$ FMQ between +1 and +2 (Richards, 2015).

The calculated fO<sub>2</sub> of the MIs determined using Fe μ-XANES and EPMA data corrected for both PEC and Fe-loss depends on whether a closed or open systemconditions were used for fO2 during the correction. In the open system scenario, both Fe2+ and Fe3+ diffuse in and out of the melt inclusion and thus the Fe<sup>3+</sup>/Fe<sub>tot</sub> ratio measured by µ-XANES remains constant. On the other hand, in a closed system scenario, only Fe<sup>2+</sup> can be modified from



 $2\sigma^{\boldsymbol{a}}$ 0.35

0.81 0.80 0.45

0.73

0.55

0.45

0.74

Fig. 7. Major element variations of the studied suite of olivinehosted MIs. The composition of the bulk volcanic products of the LHC from Salas et al. (2017) is shown for comparison, along with calculated liquid lines of descent at 1 GPa using Petrolog 3 software. The major element covariations are consistent with olivine fractionation, depicting the primitive nature of the inclusions. Bulk rock compositions are consistent with further fractionation of clinopyroxene  $\pm$  plagioclase.

the composition of the melt inclusion, and therefore the Fe<sup>3+</sup>/Fe<sub>tot</sub> ratio measured by μ-XANES increases proportionally to the amount of Fe lost during post-entrapment re-equilibration. Hence, the fO2 values calculated from the corrected composition of the MIs considering an open system behavior are higher than those resulting from a

<sup>0.13</sup> Average Std. Dev. (Ol) 0.24 0.30 0.04 0.16 \* Calculated based on Ballhaus et al. (1991) at 1 GPa.

closed system correction. We calculated the differences for both scenarios and the results are shown in Appendix 2. However, given the highly incompatible behavior of Fe<sup>3+</sup> in olivine, we consider that the original composition of the MIs should be closer to those corrected as a closed system for Fe<sup>3+</sup>; thus, we will use this compositions hereafter for further discussions.

The calculated fO<sub>2</sub> of the MIs determined using this method yields  $\Delta$ FMQ values between +1.8 and +3.6 (mean  $2.6 \pm 0.6$ ,  $1\sigma$ ) (Table 2, Appendix 2). The uncertainty related to of the MIs fO2 using this method results from three factors (1) the error in the determination of the  $Fe^{3+}/Fe_{tot}$  ratio of melt inclusions ( $\pm 0.05$ ; determined as deviation from an average value by repeatedly reducing the same spectra) (2) the analytical error in the total FeO content of the MIs obtained from the microprobe data  $(\pm 0.35, 2\sigma)$ , and (3) the error related to the calculation of the original composition of the MIs due to postentrapment modification processes. For the latter, we have added an additional error of 0.5 % of the calculated original total FeO content. Thus, the total propagated uncertainties on the calculation of the fO<sub>2</sub> of the melt inclusions from the μ-XANES data varies between 0.32 and 0.52 log units (Table 2).

Finally, we calculated the  $fO_2$  of the MIs using olivinemelt V partitioning, which yields fO<sub>2</sub> values that range from  $\Delta$ FMQ +2.2 to +3.3 (mean +2.6 ± 0.3, 1 $\sigma$ ) (Table 3), calculated using equation 5 from Shishkina et al. (2018), after obtaining the  $D_n^{ol/melt}$  for 21 different melt inclusion-olivine host pairs. The D values can be slightly affected by PEC, and therefore were corrected according to the degree of PEC of each melt inclusion (Table 3). The  $fO_2$  yielded from olivine-melt V partitioning are similar to those determined using Fe u-XANES. Each of the calculated fO<sub>2</sub> values determined by this method carry a large uncertainty related to (1) errors inherent to the experimental calibration of the partition coefficients (Shishkina et al. 2018), and (2) errors related to the analytical determination of V in the MI and olivine using LA-ICP-MS (Appendix 2). Propagation of these errors results in an averaged uncertainty of 0.9 log units (Table 3).

## 5. DISCUSSION

The MIs trapped in Mg-rich olivine crystals from the LHC basaltic tephra display major and trace element trends that are primarily indicative of olivine fractionation primarily (Fig. 7). These trends suggest that the studied MIs constitute a genetically related suite and underline their highly primitive nature. Their trace element chemistry (Fig. 2) show characteristic patterns typical of hydrous and LILErich magmas formed after melting of an initially depleted MORB-type mantle source (low HREE), with addition of slab-derived components (Schmidt and Jagoutz, 2017). Thus, the results presented here allow further exploration of the redox record of typical primitive melts that have suffered little differentiation in a mature arc setting.

The  $fO_2$  data at LHC indicate a difference in the redox state calculated using mineral equilibria vs. melt inclusions. The olivine-spinel oxybarometer yield a  $\Delta$ FMQ value of

 $+1.3 \pm 0.4$  (Table 1), while MIs Fe μ-XANES and olivine-melt V partitioning oxybarometer yield consistently higher averaged values of  $\Delta FMQ + 2.6 \pm 0.6$  (Table 2) and  $2.6 \pm 0.3$  (Table 3), respectively. Changes in the intensive variables of magmas affect the  $fO_2$  estimations derived from its Fe<sup>3+</sup>/Fe<sub>tot</sub> ratio (Kress and Carmichael, 1991). However, for instance, varying pressure between 0.1 and 1 GPa or decreasing temperature by 200 °C only results in an increase of  $\sim$ 0.15 log units with respect to the FMQ buffer, which is insignificant when considering the range of  $fO_2$  values obtained and the associated calculated uncertainties.

Therefore, a  $\sim 1.3$  log unit discrepancy in the averaged fO<sub>2</sub> values might represent either an artifact resulting from post-entrapment oxidation affecting the MIs, different stages of redox evolution recorded in the mineral phases and melt inclusion assemblages, or a potential issue in the intercalibration among methods. In addition to the PEC and Fe<sup>2+</sup> loss (see Section 4.5), there are other postentrapment diffusive processes that can further complicate the proper interpretation of fO2 determinations of olivinehosted MIs. Among these, the diffusion of H<sup>+</sup> and Fe<sup>3+</sup> to the external host and/or melt may have an impact on the redox state of the melt inclusion (Rowe et al., 2007; Gaetani et al., 2012; Bucholz et al., 2013; Hartley et al., 2015, 2017). In the next paragraphs, we discuss the potential effect of post-entrapment diffusive modification of MIs to assess the reliability of our  $fO_2$  determinations based on Fe μ-XANES and olivine-melt V partitioning.

#### 5.1. Assessing the fO<sub>2</sub> record of the LHC MIs

The degree to which post-entrapment diffusive modification processes can re-equilibrate the composition and/or oxidation state of an olivine-hosted melt inclusion, obliterating the original entrapment conditions, largely depends on the degree to which certain elements can be exchanged between the melt and host, or through the host. High diffusivities in the host crystal, higher partition coefficients between host crystal and melt, higher temperature, and smaller-sized host crystals and MIs enhance the reequilibration (Qin et al., 1992). Iron can re-equilibrate almost completely with the surrounding melt on timescales of hours to days at magmatic temperature (Gaetani et al., 2012; Bucholz et al., 2013). Even with the commonly expected magma ascent and eruption simplicity of monogenetic vents, timescales of hours to days are relatively very short considering that some systems record residence times of ~15 years (Johnson et al., 2008). Conversely, V is present at trace concentrations in the melt, has a much lower partition coefficient in olivine, and has also lower diffusivity than Fe in olivine, making it more robust to post-entrapment diffusive modifications (Oin et al., 1992).

It is important to note that  $fO_2$  values obtained for MIs using Fe  $\mu$ -XANES and corrected for PEC and Fe loss, and  $D_v^{al/melt}$  data corrected for PEC are consistent with each other. This means that, regardless of the specific mechanism, if post-entrapment diffusive re-equilibration processes altered the original  $fO_2$  values, it occurred over long time scales that resulted in the obfuscation of both the V concentration and the Fe<sup>3+</sup>/Fe<sub>tot</sub> ratio of the MIs. One way to

Table 2 Summary of data used in the estimation of  $fO_2$  based on the Fe  $\mu$ -XANES analyses

# <b>C</b>	Centroid Energy (eV)	Fe <sup>3+</sup> /Fe <sub>tot</sub> Measured	PEC (%)	$\mathrm{Fe^{3+}/Fe_{tot}}$		$Fe_2O_3 \text{ (wt.\%)}$	FeO (wt.%)	ΔFMQ	
				PEC and Fe-Loss Corrected	$2\sigma^{a}$			(1200 °C, 1 GPa)	$2\sigma^{\rm b}$
3	7112.455	0.4986	7.52	0.4632	0.0249	4.09	4.27	3.40	0.49
4	7112.300	0.4540	7.29	0.4229	0.0227	3.73	4.58	3.10	0.43
5	7112.451	0.4971	6.33	0.4788	0.0249	4.22	4.14	3.60	0.52
9	7112.144	0.4030	5.08	0.3399	0.0202	3.00	5.24	2.32	0.37
7	7112.314	0.4168	08.9	0.3658	0.0208	3.21	5.01	2.53	0.38
21	7112.253	0.3813	5.28	0.3311	0.0191	2.91	5.29	2.19	0.35
28	7112.270	0.3915	8.23	0.2877	0.0196	2.44	5.43	1.75	0.32
34	7112.426	0.4823	5.36	0.3825	0.0241	3.35	4.87	2.69	0.40
37	7112.336	0.3822	7.41	0.2919	0.0191	2.47	5.40	1.80	0.33
38	7112.336	0.4295	9.24	0.3360	0.0215	2.97	5.27	2.30	0.37

The uncertainty represents the error propagated from the determination of FeO by EPMA, the error on the determination of Fe3+/Fetot by -XANES analyses, and a conservative 0.5% error in the determination of  $\mathrm{Fe}^{3+}/\mathrm{Fe}_{\mathrm{tot}}$  in the melt inclusions related to the estimation of the original FeO of the melt inclusions.

evaluate this effect involves calculating the degree of V reequilibration that can occur over time. We used to the model of Oin et al. (1992) to estimate V re-equilibration timescales under different  $\Delta FMQ$  conditions. A melt inclusion with a diameter of 80 µm and an olivine host of 800 µm was used, consistent with our samples. Vanadium diffusivity values were taken from Spandler and O'Neill (2010) and the  $D_n^{ol/melt}$  data from Shishkina et al. (2018). Fig. 8 shows the results of the modelling, suggesting that significant V reequilibration (~80%) will occur after two years at  $\Delta FMQ = 0$ , and after four years at  $\Delta FMQ = +2$ . In contrast, complete V re-equilibration will occur only after approximately five years. It is important to highlight that the V diffusivity data of Spandler and O'Neill (2010) were obtained at 1300 °C and therefore the re-equilibration times can be considered as conservative.

Our second approach involved assessing whether postentrapment modifications could have sufficiently reequilibrated V concentrations within the olivine-hosted MIs. Necessarily, V diffusion timescales would have needed to be longer than the residence time of magma prior to eruption. We estimated residence times by means of Mg-Fe diffusion modelling on olivine crystal rims. Iron and Mg concentration profiles were measured in 8 olivine crystals from the LHC tephra material using EMPA. All the olivine crystals used for diffusion modelling were carefully selected according to the criteria described in Costa et al. (2008) and Shea et al. (2015). Two 1D traverse measurements in one crystal plane were used for verifying the obtained timescales (Fig. 9) from single olivine crystals (Shea et al., 2015). The internal buffered shape of the compositional profiles (Fig. 9) and the coincidence of the timescales also ensure that the diffusion-related gradients are valid and not associated with an external control (Costa et al., 2008). To obtain high-resolution traverses, we coupled the EMPA measurements with the backscattered electron (BSE) images and back-scattered electron diffraction data (BSED). This method has been used successfully in previous studies (e.g., Martin et al., 2008; Hartley et al., 2016; Morgado et al., 2017; Pankhurst et al., 2018), and allows obtaining diffusion data irrespective of the crystallographic orientation of the olivine crystal section in the sample. We calculated diffusion coefficients along [0 0 1] direction in olivine phenocrysts using the equations of Dohmen and Chakraborty (2007). In addition, we calculated the uncertainties in diffusion coefficient and consequent magmatic timescales following the procedure of Kahl et al. (2015). The latter method considers errors in the calculated temperature and  $fO_2$ . Calculations were made for a temperature of 1300 °C ( $\pm$ 30 °C), and a pressure of 0.2 GPa at  $\Delta$ FMQ = +1. Modelled results obtained solving Fick's second law for each profile diffusion coefficient resulting from its crystallographic orientation and obtained according to Philibert (1991). The calculated residence time vielded scales varying from 13 to 102 days (uncertainty of up to ~100 days), which can extend up to 204 days considering changes resulting from increasing pressure to values as high as 1.5 GPa. In Fig. 9, two diffusion profiles yielding 38 and 52 days are shown (details in Table 4; also, the residence time interval is shown in Fig. 8 as a reference).

Table 3 Vanadium concentration of MIs and their olivine host data used for the olivine-melt vanadium oxybarometry.

Inclusion #	PEC (%) <sup>a</sup>	Vanadium in melt inclusions (μg·g <sup>-1</sup> )		Vanadium in olivine (μg·g <sup>-1</sup> )	Olivine/melt V patitioning		Oxygen fugacity estimates	
	Measured PEC-corrected <sup>b</sup>			D <sub>V</sub> ol/melt	$2\sigma^{c}$	ΔFMQ	$2\sigma^{d}$	
43	9.86	320	288	4.3	0.0149	0.0059	2.3	0.9
62	3.43	309	298	4.4	0.0147	0.0059	2.3	0.9
103	5.51	299	283	4.1	0.0144	0.0059	2.3	0.9
91	1.08	302	299	4.2	0.0141	0.0058	2.3	0.9
55	9.59	276	250	3.7	0.0148	0.0059	2.3	0.9
110	3.67	198	191	2.6	0.0136	0.0059	2.4	0.9
92	4.79	241	229	3.1	0.0135	0.0058	2.4	0.9
76	3.73	280	270	3.5	0.0130	0.0058	2.5	0.9
1	8.54	274	251	3.3	0.0132	0.0058	2.4	0.9
102	3.45	304	294	3.5	0.0119	0.0058	2.6	0.9
47	4.00	278	267	3.2	0.0120	0.0057	2.6	0.9
72	2.46	325	317	3.5	0.0110	0.0057	2.7	0.9
31	8.90	314	286	3.4	0.0119	0.0056	2.6	0.9
32	14.36	318	272	3.4	0.0125	0.0057	2.5	0.9
106	2.72	259	252	2.6	0.0103	0.0056	2.8	0.9
90	0.67	305	303	3.0	0.0099	0.0056	2.8	0.9
19	11.38	270	239	2.3	0.0096	0.0055	2.9	1.0
40	13.46	297	257	2.4	0.0093	0.0055	2.9	1.0
3	7.52	265	245	2.1	0.0086	0.0055	3.0	1.0
8	5.49	311	294	2.0	0.0068	0.0054	3.3	1.0
Average		287	269	3.2	0.0120	0.0057	2.6	0.9

a Post-entrapment crystallization of olivine along the rims of the melt inclusion as calculated from Petrolog software.

b Correction applied to the melt inclusions to obtain their V concentration before PEC occurred.

c Uncertainty associated to the D<sub>V</sub>O/melt derived from the analytical error in the determination of the V content of olivine and melt by LA-ICP-MS. Calculated using a conventional rule for error

d Uncertainty associated to the calculation of ΔFMQ values considering both analytical and methodological errors associated to their calibration.

Using these data, we proceeded to compare the time scales needed for V re-equilibration with time scales of magmatic residence. As seen in Fig. 8, the calculated times of residence of the LHC magma in the crust (<204 days) is far too short compared to the 2 years needed for significant vanadium re-equilibration to occur (~80%) at  $\Delta FMQ = 0$ . Therefore, our modelled data confirm that the  $D_v^{ol/melt}$  values were not significantly affected by post-entrapment diffusive re-equilibration processes. This result strongly suggests that the  $fO_2$  values calculated using V partitioning data and Fe $\mu$ -XANES are representative of the original redox state of the MIs and differ from the  $fO_2$  recorded in the mineral phase assemblage. The potential implications are discussed in the next section.

#### 5.2. Oxidation of LHC magmas

Primitive basaltic melts have been widely used to constrain the oxidation state of the mantle (Evans et al., 2012). However, the ability of primitive melts to record the oxidation state of their mantle source has been questioned (e.g., Lee et al., 2005, 2010). It is likely that, if primary basaltic melts evolve from their original fO2 condition during ascent toward the surface, the calculated  $fO_2$  of magmas would not be directly representative of their mantle source. It is commonly assumed that because of the primitive nature of some basalts, differentiation could have not significantly altered their original (primary) redox conditions. However, only a few studies have attempted to constrain the effects of magmatic differentiation on the redox state of primitive magmas (Kelley and Cottrell, 2012; Hartley et al., 2017), and none of them on samples from mature arc settings.

The oxidation state of the LHC magmas recorded by the olivine-spinel equilibrium shows relatively common conditions for arc magmas; i.e., slightly more oxidized than

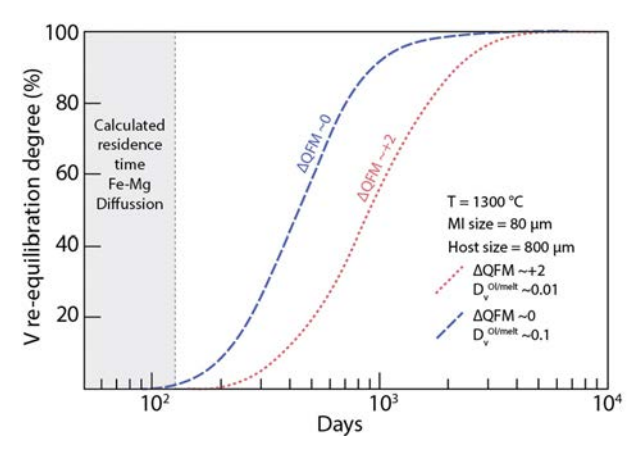


Fig. 8. Vanadium (V) re-equilibration timescales between olivine-hosted MIs and carrier melt at  $1300\,^{\circ}\text{C}$  and variable  $f\text{O}_2$  conditions. Calculations were based on the model by Qin et al. (1992) and modified after Shishkina et al., (2018). The residence time of the LHC magma prior to eruption, calculated using Mg-Fe diffusion in olivine (Fig. 8), is shown for comparison. The data highlights that residence time (<200 years) was significantly short for V to re-equilibrate.

MORBs. However, the fO2 recorded by the melt inclusion assemblage are up to ~1.3 orders of magnitude more oxidized (Tables 1-3). Considering that post-entrapment processes did not significantly alter the fO2 of the melt inclusions, one alternative is that the fO2 data at LHC record different stages of a process of redox evolution. Under this scenario, our data would be indicative of fO<sub>2</sub> conditions of  $\Delta FMQ = +1.3 \pm 0.4$  during the equilibration of olivine and Cr-spinel, and  $\Delta FMQ = +2.6 \pm 0.6$  during the entrapment of the MIs. However, it is unlikely that all the Cr-spinel-olivine pairs equilibrated at lower fO<sub>2</sub> and all the MIs trapped at a relatively higher fO2. Thus, our data shows a complex redox record with a discrepancy between the  $fO_2$  estimated by the crystal assemblage and the  $fO_2$  values obtained from the melt inclusions. This disparity potentially represents a mismatch in the intercalibration between different methods, opening an important avenue of research that requires further attention.

Interestingly, the calculated  $fO_2$  of the MIs analyzed by Fe μ-XANES increases with progressive differentiation of the melts. Fig. 10A and B show that the calculated  $\Delta$ FMQ values increase progressively from +1.8 at 47.2 wt.% SiO<sub>2</sub> and 18 wt.% Al<sub>2</sub>O<sub>3</sub> to +3.6 at 50.9 wt.% SiO<sub>2</sub> and 16.3 wt.% Al<sub>2</sub>O<sub>3</sub>. Thus, the most differentiated silica rich melt inclusions are more oxidized than the most primitive melt ones. The latter is strongly suggesting that a case of oxidation during magmatic evolution is recorded in the LHC olivine-hosted melt inclusions. Noteworthy, these trends are also present when the composition of the melt inclusions using an open system for Fe<sup>3+</sup>/Fe<sub>tot</sub> is considered (Appendix 2). The decreasing Al<sub>2</sub>O<sub>3</sub> trend during differentiation recorded by the MIs might be most simply explained by plagioclase crystallization. However, although plagioclase can be found in the basaltic lava flows from the LHC, it is absent in the tephra material of their eruptive stages studied here (as also confirmed by Salas et al., 2017). In addition, it is difficult to reconcile how the explosive stages of volcanism would have selectively erupted oliand not plagioclase. Therefore plagioclase crystallization could not have been responsible for the progessive increase in the Al<sub>2</sub>O<sub>3</sub> content of the MIs.

To further evaluate the case of oxidation during magmatic evolution, we inspected the trace elements composition of the melt inclusions and the olivine-melt vanadium partitioning redox calculations. Having calculated the fO<sub>2</sub> of the LHC system and its melt inclusions, it is possible to address whether they reflect the oxidation state of their mantle source. Redox-sensitive trace element ratios such as V/Sc have been used as  $fO_2$  tracers of the mantle source region of magmas. The redox-dependent partitioning of V between crystallizing phases and melt and its incompatible behavior during partial melting renders the potential of the V/Sc tracer as an oxybarometer (Lee et al., 2005). At higher fO2, V becomes more incompatible and therefore, upon partial melting of the mantle, magmas will acquire a higher V/Sc ratio. Lee et al. (2005) argued that the oxidation state of the source of mid ocean ridge basalts (MORBs) and arcrelated magmas is undistinguishably low ( $\Delta$ FMQ <  $\pm$ 0.25). However, this hypothesis was recently challenged by Wang et al. (2019). The aforementioned authors proposed that the

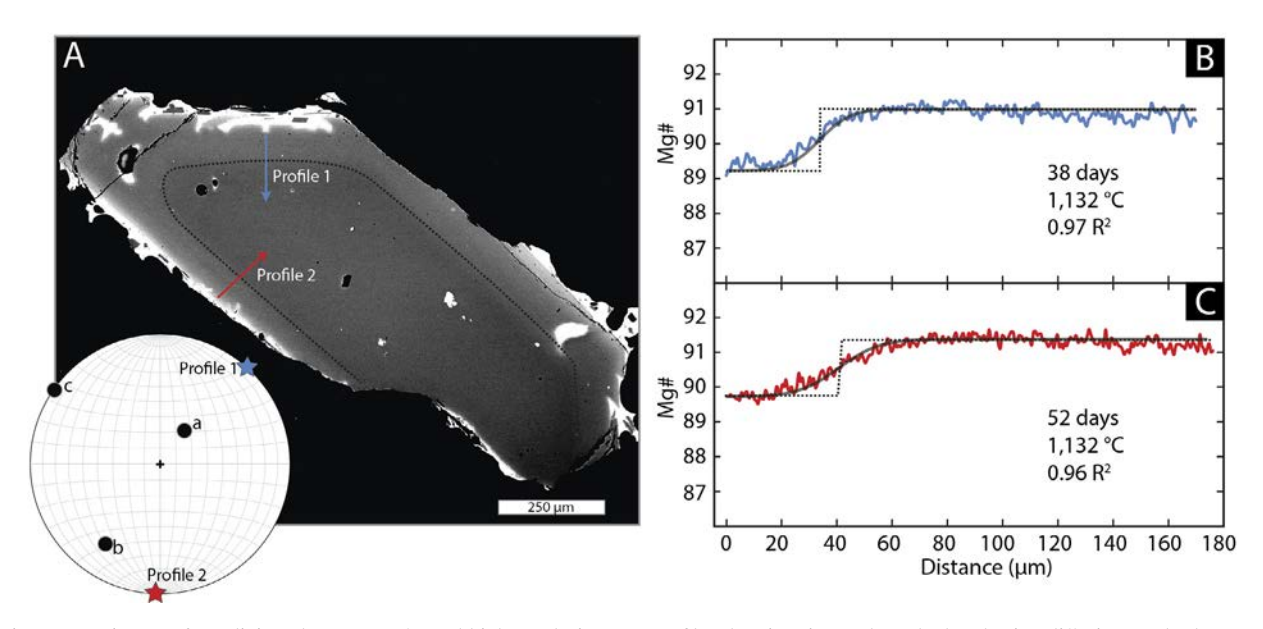


Fig. 9. BSE image of an olivine phenocryst (A) and high-resolution Mg profiles showing timescales calculated using diffusion methods (B, C). The crystallographic orientation (axis a, b, and c) and traverse directions projected onto the stereographic lower hemisphere are shown in (A). (B) and (C) show the Mg# content of the high-resolution profiles calculated from BSE grayscale calibrated profile plotted against distance. Colored lines: BSE profiles; solid dark line: best fit diffusion model (highest coefficient determination, R<sup>2</sup>) between BSE profile and the Mg# content measured; dashed line: initial forsterite profile.

Table 4
Representative timescales calculated in individual olivine crystals.

Sample ID	$D (m^2/s)$	t (average)	t (min)	t (max)	$\mathbb{R}^2$
Cx-1A p1	8.44E-17	63	30	118	0.98
Cx-1A p2	7.89E - 17	62	41	129	0.95
Cx-1B p1	9.14E - 17	13	9	26	0.97
Cx-1A p2	1.52E-17	22	15	45	0.90
Cx-3A p1	1.58E-17	38	26	63	0.97
Cx-3A p2	1.52E-17	52	37	115	0.96
Cx-3C pl	1.68E-17	54	42	105	0.96
Cx-3C p2	1.81E-17	73	51	166	0.90
Cx-4B p1	4.89E - 17	38	27	63	0.99
Cx-4B p2	3.77E-17	38	27	64	0.99
Cx-4D p1	3.18E-17	102	69	215	0.93
Cx-4D p2	1.40E - 17	90	62	151	0.96
Cx-6D p1	4.32E-17	25	21	67	0.97
Cx-4D p2	1.56E-17	28	18	58	0.98

t is time in days.

temperature-dependent partitioning of V coupled with the relatively lower temperature of arc magmas compared to MORBs indicate that the source of arc magmas should be 1 log unit above that of MORBs. This suggest that the choice of partitioning values as well as the temperature are critical parameters to consider in order to modelling V/Sc ratios of partial melts. In addition, Bucholz and Kelemen (2019) showed that the modal composition and source V/Sc ratios are also fundamental for assessing the  $fO_2$  of the mantle source of magmas. The low HREE concentration of the LHC MIs (Fig. 2) indicates that its mantle source is more depleted than that of MORBs, as typical for arc magmas (Schmidt and Jagoutz, 2017). Therefore, here we modelled the V/Sc ratios of magmas upon non-modal

batch melting of a depleted arc-like source by using two different sets of V partitioning values. The source has a modal composition of 66.3% olivine, 8.7% clinopyroxene, 20.6% orthopyroxene, and 4.4% spinel, and the initial V/Sc is 4.9 as derived from the average V/Sc ratio in peridotite xenoliths from arcs (Bucholz and Kelemen, 2019). Fig. 11A shows the results of modelling using the V and Sc mineral-melt partitioning values of Mallmann and O'Neill (2009). Fig. 11B shows the results of modelling using the values of Wang et al. (2019) at 1200 °C and 1300 °C (see figure caption for details on the calculation of V<sup>mineral/melt</sup> partition coefficients). Fig. 11 shows that the modelling using the partitioning values of Wang et al. (2019) results in higher fO2 values for a certain degree of partial melting and V/Sc ratio, in agreement with their interpretations. The average V/Sc ratio of the MIs studied here is  $7.66 \pm 1.58$  (1 $\sigma$ ) (Fig. 11). These values are similar to the most frequent values for arc and MORBs (Stolper and Bucholz, 2019). Typical degrees of partial melting beneath arcs are between 15 and 20% (Stolper and Newman, 1994; Kelley et al., 2006). Considering a 15-20% degree of partial melting for the studied MI and using average V/Sc ratios of the studied MIs, our modelling suggests that the mantle source of the LHC magmatic system vary between  $\Delta FMQ + 0.7$  and  $\Delta FMQ + 2$ . Although these values represent a wide range, they are in agreement with those obtained via Cr-spinel-olivine equilibrium (Ballhaus et al., 1991) and are below average values obtained via olivine-melt vanadium partitioning (Shishkina et al., 2018) and Fe  $\mu$ -XANES.

Fig. 12 compares the  $fO_2$  values revealed by melt inclusion and obtained via their V/Sc ratios and the modelling, and olivine-melt vanadium partitioning. It is important to highlight that whereas V/Sc approach reflects the  $fO_2$  at

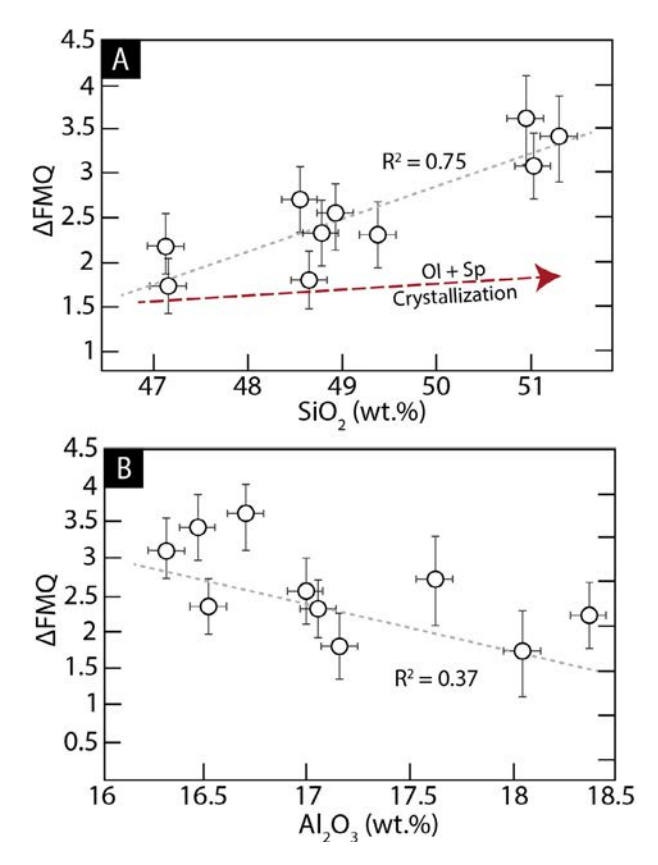


Fig. 10. Major element variations of the olivine-hosted melt inclusions plotted against their calculated  $fO_2$  values based on the  $Fe^{3+}/Fe_{tot}$  values determined by  $Fe\ \mu$ -XANES. The uncertainty on the X axis is derived from the EPMA. The uncertainty on the Y axis is calculated by propagating that of the  $\mu$ -XANES, EPMA, and that derived from post-entrapment modifications correction. (A) Shows the  $SiO_2$  wt.% against  $\Delta FMQ$  and (B) shows the  $Al_2O_3$  wt.% against  $\Delta FMQ$  values for each analyzed melt inclusion. The red dotted line in (A) represents the  $\Delta FMQ$  evolution of the melt resulting from the crystallization of olivine and spinel modelled using Petrolog 3 software at 1 GPa.

the source from which they derive, the olivine-melt vanadium partitioning reflects the  $fO_2$  conditions at the time of the entrapment of the MIs (i.e., after leaving their mantle source). Therefore, the 1:1 line on Fig. 12 represents a melt that evolved closed to  $fO_2$  from their formation at the mantle source to the later crystallization of olivine at shallower levels. This comparison reveals that the data falls below the equiline, indicating that the studied melts suffered oxidation after leaving their mantle source (Fig. 12). Average values from Fig. 12 indicates that the melt inclusions were oxidized by 1.3 log units in  $fO_2$  after leaving their mantle source. These results are in agreement with the  $fO_2$  of the melt inclusions revealed by their Fe  $\mu$ -XANES data (Fig. 10), strongly suggesting that the melt inclusions record a process of oxidation during differentiation.

# 5.3. Oxidation mechanisms during the evolution of primitive arc melts

Oxidation of primitive arc magmas during ascent can be caused by assimilation of more oxidized crustal rocks,

which can remain unnoticed in primitive arc melts (Schmidt and Jagoutz, 2017). However, rocks that have experienced assimilation have also been shown to be more reduced (Ague and Brimhall, 1988), indicating that crustal assimilation would not unequivocally promote oxidation. Although we cannot quantify this effect, we expect it to be relatively minor considering that the short magmatic residence times calculated for the LHC eruptive products using Mg-Fe diffusion models in olivine (<204 days; Fig. 9) points towards little potential to fully incorporate significant crustal material.

Magma oxidation can also result from early crystallization of Fe<sup>2+</sup>-bearing phases such as olivine and Cr-spinel, increasing the Fe<sup>3+</sup>/Fe<sub>tot</sub> ratio of the remaining melt. In the LHC, it is likely that crystallization of both olivine and Cr-spinel could have increased the Fe<sup>3+</sup>/Fe<sub>tot</sub> ratio of the remaining melt, given that both mineral phases have lower Fe<sup>3+</sup>/Fe<sup>2+</sup> ratios than the silicate melt (Appendix 2 and 2). In order to quantify this effect, we modelled the evolution of the Fe<sup>3+</sup>/Fe<sub>tot</sub> ratio of the melt due to the crystallization of olivine and spinel using Petrolog3 software and keeping the system open to fO2. The results of this modelling indicate that even after reaching values as low as 4 wt.% MgO, the ΔFMO values of the system only increase by 0.4 log units. Fig. 10 shows the results of modelling the redox evolution of magmas upon crystallization of olivine and spinel for the range studied MIs composition. Our results are in agreement with previous estimations performed by Cottrell and Kelley (2011) demonstrate that the crystallization of Fe<sup>2+</sup>-bearing phases alone is alone insufficient to explain the fO<sub>2</sub> differences observed here.

Another possibility is related to sulfur degassing during ascent and storage. Sulfur outgassing occurs predominantly as SO<sub>2</sub>, whereas the S redox equilibria in basaltic melts is controlled by S<sup>6+</sup> and/or S<sup>2-</sup> species (Oppenheimer, 2003; Wallace, 2005; Metrich et al., 2009; Jugo et al., 2010). Considering the fact that the LHC MIs were among the most affected by degassing of the entire SVZ (Wehrmann et al., 2014) and that calculated fO2 values point to predominantly S<sup>6+</sup> species in the melt (Jugo et al., 2010), it is possible that S degassing might have caused oxidation of the remaining melt. In fact, the three most oxidized inclusions having Fe-XANES data display lower S contents compared to the least oxidizes ones, suggesting that S degassing might have caused some oxidation. However, the devolatilization of 1000  $\mu g \cdot g^{-1}$  of S can result in the oxidation of 0.35% Fe<sup>2+</sup> to Fe<sup>3+</sup>, which translates to a variation in the  $fO_2$  of the magmas of only  $\Delta FMQ \sim 0.3$ . Therefore, the effect of S degassing alone cannot explain the redox evolution observed at LHC.

The  $fO_2$  increase at LHC likely resulted from a combination of the mentioned processes rather than a single factor. However, the extent of such processes remains unknown and therefore there is insufficient evidence to fully explain the reportedly large redox variations. An important aspect worth mentioning here is that the large gradients in  $fO_2$  recorded in the LHC eruptive products occurred despite the very limited geochemical evolution of the studied melts (i.e., Mg# of the studied olivine between 87.7 and 92.5). The Mg# of olivine is commonly used to determine whether

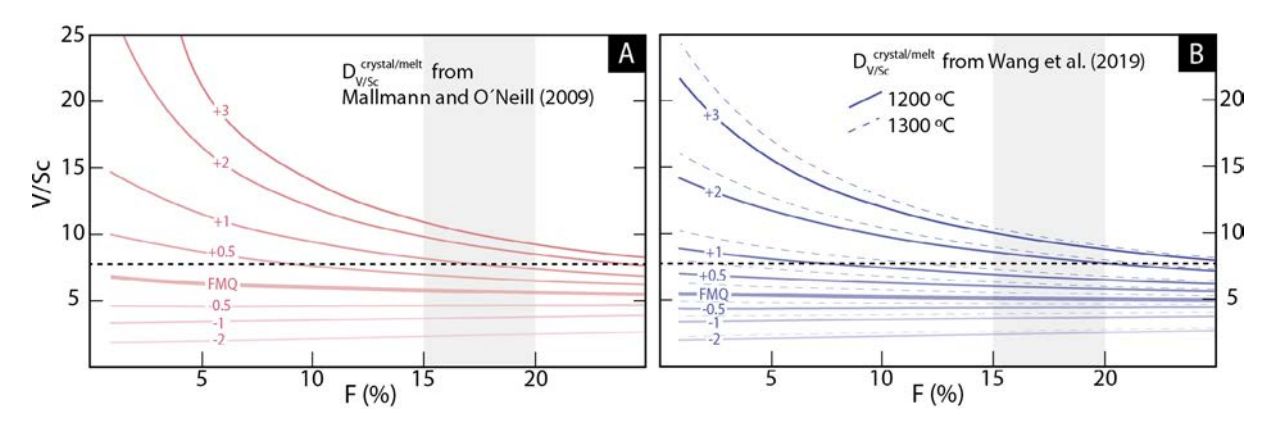


Fig. 11. Modelled V/Sc ratios of melts produced at variable  $fO_2$  by non-modal batch melting of depleted mantle source with 66.3% olivine, 8.7% clinopyroxene, 20.6% orthopyroxene, and 4.4% spinel. Source V/Sc is 4.9 as derived from the average V/Sc ratio in peridotite xenoliths from arcs (Bucholz and Kelemen, 2019). (A) Shows the results of modelling using V and Sc partitioning data of Mallmann and O'Neill (2009). (B) Shows the results of modelling using V and Sc partitioning data of Wang et al. (2019). Parameters for calculating the V partition coefficient are: 0.083 a.p.f.u. Al in clinopyroxene, 0.067 a.p.f.u. Al in orthopyroxene, 0.2 Cr# in spinel, and NBO/T = 0.7 where NBO is non-bridging oxygen (degree of polymerization).

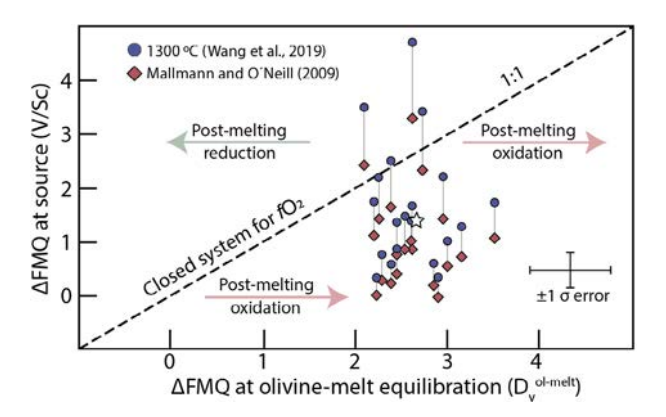


Fig. 12. Source  $fO_2$  conditions determined from V/Sc ratios plotted against the  $fO_2$  conditions revealed by olivine melt vanadium partitioning for individual olivine-hosted melt inclusions. The white star represents an average value. Values to the right of the 1:1 line indicate that the melts experienced oxidation after leaving their mantle source.

a magma is sufficiently primitive to be in equilibrium with a peridotite source (e.g., Evans et al., 2012). Our observations show that even at high Mg# and apparent equilibrium with a peridotite source, the redox state of primitive arc magmas may vary significantly, raising a cautionary note on the direct use of primitive arc melts as tracers of fO2 of the sub-arc mantle. Finally, one aspect that needs to be addressed in future studies relates to potentially fundamental intercalibration issues related to the methodologies used to constrain fO2. Although we acknowledge that some of the differences observed between oxybarometers could possibly be related to the aforementioned complication, it is important to notice that the processes of fO2 increase at LHC are also observed within single oxybarometric approaches (Figs. 10 and 12). Thus, we are confident that the effect of this potential issue will not change the main conclusions of this study. Additionally, although it is beyond the scope of this study, our data encourage future studies assessing the potential issues of the intercalibration among the different oxybarometers.

An important question that arises from the previous discussion is how can the melt  $fO_2$  increase significantly while maintaining equilibrium with a peridotite source? The answer to this question is not trivial and might be obscured by our relative lack of knowledge of the processes that affect magmas from their formation in the asthenosphere and during ascent across the deep lithosphere (lithospheric mantle and lower crust). We speculate that the differentiation of ascending melts and/or interaction with surrounding wall-rock throughout the deep lithosphere might be related to their fO<sub>2</sub> increase (e.g., Tollan and Hermann, 2019). Importantly, if the entire range of observed fO2 increase had occurred during interaction with a peridotite wall-rock (i.e., lithospheric mantle), the V/Sc ratios could have been potentially re-equilibrated, obscuring the effects observed in Fig. 12. Therefore, although the rates of V/Sc re-equilibration would likely be lower than the redox re-equilibration, some of the oxidation must have occurred during melt ascent through the crust. Thus, the open system behavior of magmas with respect to fO2 during ascent across the deep lithosphere could potentially explain some of the apparently contradictory evidence concerning the redox state of the mantle source of primitive melts, opening new avenues for the investigation of the redox state of arc magmas.

### 6. CONCLUSIONS

In this study we explored the redox record of the basaltic tephra from Los Hornitos cones (LHC) in central-southern Chile, which are among the most primitive materials reported in the Southern Volcanic Zone of the Andes with a Mg# = 92.5 and a Ni content of up to 5000  $\mu g \cdot g^{-1}$ . Oxygen fugacity determined by using mineral equilibria and melt inclusion assemblages yielded significant variances in the calculated redox conditions. Olivine-spinel oxybarometry yielded  $fO_2$  values ranging from  $\Delta FMQ$  +1.3  $\pm$  0.4, while the olivine-hosted MIs record more oxidizing conditions.  $fO_2$  values calculated based on in-situ Fe  $\mu$ -XANES

analyses yielded values from  $\Delta FMQ + 2.6 \pm 0.6$ , in agreement with the calculated fO2 values based on the olivine-melt vanadium partitioning ( $\Delta FMQ + 2.6 \pm 0.3$ ). Correlations between the major element composition of MIs and their fO<sub>2</sub> determined by Fe μ-XANES reveals a case of significant oxidation during differentiation. Assessment of the mantle source oxidation state based on V/Sc modelling and MIs data, and comparison with individual olivine-melt partitioning  $fO_2$  estimations also suggest that the LHC magmas suffered significant oxidation after leaving their mantle source. We conclude that the  $fO_2$  values of the LHC primitive melts were most likely imprinted during progressive stages of magma evolution. Although the early crystallization of olivine and Cr-spinel, and to lesser extent sulfur degassing may have contributed to oxidation of the residual melt, they are insufficient to explain the observed fO<sub>2</sub> increase. We hypothesize that the reported fO<sub>2</sub> increase during differentiation may result from a combination of redox processes in the deep lithosphere. Finally, this study shows that primitive arc melts can behave as a system open to fO<sub>2</sub> during their early geochemical evolution. Thus, regardless of the mechanisms leading to the observed redox evolution, our data provide a cautionary note on the interpretation of calculated fO2 values.

### **Declaration of Competing Interest**

The authors declare that they have no known competing financial interests or personal relationships that could have appeared to influence the work reported in this paper.

### ACKNOWLEDGEMENTS

We are deeply grateful for thorough reviews from Maxim Portnyagin, Claire E. Bucholz, and Giada Iacono-Marziano. We also thank Zoltan Zajacz for his insightful comments and editorial handling of the manuscript. This study was funded by the Iniciativa Científica Milenio, through grant "Millennium Nucleus for Metal Tracing along Subduction". Additional support was provided by the FONDAP project 15090013 "Centro de Excelencia en Geotermia de Los Andes, CEGA", and CONICYT-FONDEQUIP grants EQM120098 and EQM140009. We thank Tony Lanzirotti and Matt Newville for assistance with µ-XANES analyses at the GeoSoilEnviroCars (Sector 13), Advanced Photon Source (APS), Argonne National Laboratory. We are also grateful to Owen Neill for assistance during EPMA acquisition, to Rurik Romero for assistance during LA-ICP-MS analysis, and to Gerd Siefeld and José Tomás Ovalle for assistance and guidance during fieldwork. We acknowledge CONICYT support through PhD scholarships (#21170857, ST and #72160268, EM). This research used resources of the Advanced Photon Source, a U.S. Department of Energy (DOE) Office of Science User Facility operated for the DOE Office of Science by Argonne National Laboratory under Contract No. DE-AC02-06CH11357. Adam Simon, Brian Konecke, and Adrian Fiege acknowledge funding from National Science Foundation EAR 1524394.

# APPENDIX A. SUPPLEMENTARY MATERIAL

Supplementary data to this article can be found online at https://doi.org/10.1016/j.gca.2020.01.042.

#### REFERENCES

- Ague J. J. and Brimhall G. H. (1988) Magmatic arc asymmetry and distribution of anomalous plutonic belts in the batholiths of California: effects of assimilation, crustal thickness, and depth of crystallization. Geol. Soc. Am. Bull. 100, 912–927.
- Anderson, Jr., A. T. and Brown G. G. (1993) CO<sub>2</sub> contents and formation pressures of some Kilauean melt inclusions. Am. Mineral. 78, 794–803.
- Ballhaus C., Berry R. F. and Green D. H. (1991) High pressure experimental calibration of the olivine-orthopyroxene-spinel oxygen geobarometer: implications for the oxidation state of the upper mantle. *Contrib. Miner. Petrol.* **107**, 2279–2302.
- Ballhaus C., Berry R. F. and Green D. H. (1994) High-pressure experimental calibration of the olivine-orthopyroxene-spinel oxygengeobarometer: implications for the oxidation state of the upper mantle. *Contrib. Miner. Petrol.* **118**, 109.
- Berman R. G. (1998) Internally-consistent thermodynamic data for minerals in the system Na<sub>2</sub>O-K<sub>2</sub>O-CaO-MgO-FeO-Fe<sub>2</sub>O<sub>3</sub>-Al<sub>2</sub>O<sub>3</sub>-SiO<sub>2</sub>-TiO<sub>2</sub>-H<sub>2</sub>O-CO<sub>2</sub>. *J. Petrol.* **29**, 445–522.
- Berry A. J., O'Neill H., St C., Jayasuriya K. D., Campbell S. J. and Foran G. J. (2003) XANES calibrations for the oxidation state of iron in a silicate glass. *Am. Mineral.* **88**, 967–977.
- Borisov A. A., Kadik A. A., Zharkova Y. V. and Kalinichenko N. V. (1987) Effects of oxygen fugacity on the ration between valency forms of vanadium in magmas. *Geochem. Int.* 24, 111–116 (translated from Geokhimiya 6, 892-897).
- Bouvier A.-S., Manzini M., Rose-Koga E. F., Nichols A. R. L. and Baumgartner L. P. (2019) Tracing of Cl input into the sub-arc mantle through the combined analyses of B, O and Cl isotopes in MIs. *Earth Planet. Sci. Lett.* **507**, 30–39.
- Brandon A. D. and Draper D. S. (1996) Constraints on the origin of the oxidation state of mantle overlying subduction zones: An example from Simcoe, Washington, USA. Geochim. Cosmochim. Acta 60, 1739–1749.
- Bucholz C. E. and Kelemen P. B. (2019) Oxygen fugacity at the base of the Talkeetna arc, Alaska. *Contrib. Mineral. Petrol.* **174**, 79.
- Bucholz C. E., Gaetani G. A., Behn M. D. and Shimizu N. (2013) Post-entrapment modification of volatiles and oxygen fugacity in olivine-hosted MIs. *Earth Planet. Sci. Lett.* 374, 145–155.
- Canil D. and Fedortchouk Y. (2001) Olivine-liquid partitioning of vanadium and other trace elements, with applications to modern and ancient picrites. *Can. Mineral.* **39**, 319–330.
- Cannatelli C., Doherty A. L., Esposito R., Lima A. and De Vivo B. (2016) Understanding a volcano through a droplet: a melt inclusion approach. J. Geochem. Explor. 171, 4–19.
- Chen Y., Provsot A., Schiano P. and Cluzel N. (2011) The rate of water loss from olivine-hosted MIs. *Contrib. Miner. Petrol.* 162, 397–411.
- Cherniak D. J. (2010) REE diffusion in olivine. *Am. Mineral.* **95**, 362–368.
- Condie K. C. (1993) Chemical composition and evolution of the upper continental crust: contrasting results from surface samples and shales. *Chem. Geol.* **104**, 1–37.
- Costa F., Dohmen R. and Chakraborty S. (2008) Time scales of magmatic processes from modeling the zoning patterns of crystals. Rev. Mineral. Geochem. 69, 545–594.
- Cottrell E. and Kelley K. A. (2011) The oxidation state of Fe in MORB glasses and the oxygen fugacity of the upper mantle. *Earth Planet. Sci. Lett.* **305**, 270–282.
- Cottrell E., Kelley K. A., Lanzirotti A. and Fischer R. A. (2009) High-precision determination of iron oxidation state in silicate glasses using XANES. *Chem. Geol.* 268, 167–179.
- Cottrell E., Lanzirotti A., Mysen B., Birner S., Kelley K. A., Botcharnikov R., Davis F. A. and Newville M. (2018). Am. Mineral.: J. Earth Planet. Mater. 103(4), 489–501.

- Danyushevsky L. V. and Plechov P. (2011) Petrolog3: integrated software for modeling crystallization processes. *Geochem., Geophys. Geosyst.* **12.** 1–32.
- Danyushevsky L. V., Della-Pasqua F. N. and Sokolov S. (2000) Re-equilibration of MIs trapped by magnesian olivine phenocrysts from subduction-related magmas: Petrological implications. *Contrib. Miner. Petrol.* 138, 68–83.
- Danyushevsky L. V., McNeill A. W. and Sobolev A. V. (2002) Experimental and petrological studies of MIs in phenocrysts from mantle-derived magmas: an overview of techniques, advantages and complications. *Chem. Geol.* 183, 5–24.
- Dauphas N., Craddock P. R., Asimow P. D., Bennett V. C., Nutman A. P. and Ohnenstetter D. (2009) Iron isotopes may reveal the redox conditions of mantle melting from Archean to Present. *Earth Planet. Sci. Lett.* 288, 255–267.
- Davis F. A., Cottrell E., Birner S. K., Warren J. M. and Lopez O. G. (2017) Revisiting the electron microprobe method of spinel-olivine-orthopyroxene oxybarometry applied to spinel peridotites. *Am. Mineral.* 102, 421–435.
- DeMets C., Gordon R. and Argus D. F. (2010) Geologically current plate motion. Geophys. J. Int. 181, 1–80.
- Dohmen R. and Chakraborty S. (2007) Fe–Mg diffusion in olivine II: point defect chemistry, change of diffusion mechanisms and a model for calculation of diffusion coefficients in natural olivine. *Phys. Chem. Miner.* 34, 409–430.
- Dohmen R., Becker H. W. and Chakraborty S. (2007) Fe-Mg diffusion in olivine I: experimental determination between 700 and 1,200 °C as a function of composition, crystal orientation and oxygen fugacity. *Phys. Chem. Miner.* 34, 389–407.
- Ducea M. N., Saleeby J. B. and Bergantz G. (2015) The architecture, chemistry, and evolution of continental magmatic arcs. Annu. Rev. Earth Planet. Sci. 43, 299–331.
- Evans K. A., Elburg M. and Kamenetsky V. S. (2012) Oxidation state of the subarc mantle. *Geology* **40**, 783–786.
- Farges F., Lefrère Y., Rossano S., Berthereau A., Calas G. and Brown G. E. (2004) The effect of redox state on the local structural environment of iron in silicate glasses: a combined XAFS spectroscopy, molecular dynamics, and bond valence study. J. Non-Cryst. Solids 344, 176–188.
- Fiege A., Ruprecht P., Simon A. C., Bell A. S., Göttlicher J., Newville M., Lanzirotti T. and Moore G. (2017) Calibration of Fe XANES for high-precision determination of Fe oxidation state in glasses: comparison of new and existing results obtained at different synchrotron radiation sources. *Am. Mineral.* 102, 369–380.
- Ford C. E., Russel D. G., Craven J. A. and Fisk M. R. (1983) Olivine-liquid equilibria: temperature, pressure and composition dependence of the crystal/liquid cation partition coefficients for Mg, Fe<sup>2+</sup>, Ca and Mn. *J. Petrol.* **24**, 256–266.
- Gaetani G. and Grove T. (1997) Partitioning of moderately siderophile elements among olivine, silicate melt, and sulfide melt: constraints on core formation in the Earth and Mars. Geochim. Cosmochim. Acta 61, 1826–1846.
- Gaetani G. A., O'Leary J. A., Shimizu N., Bucholz C. E. and Newville M. (2012) Rapid reequilibration of H<sub>2</sub>O and oxygen fugacity in olivine-hosted MIs. *Geology* **40**, 915–918.
- Gaillard F., Scaillet B., Pichavant M. and Iacono-Marziano G. (2015) The redox geodynamics linking basalts and their mantle sources through space and time. *Chem. Geol.* 418, 217–233.
- Galoisy L., Calas G. and Arrio M. A. (2001) High-resolution XANES spectra of iron in minerals and glasses: structural information from the pre-edge region. *Chem. Geol.* 174, 307– 319.
- Gavrilenko M., Herzberg C., Vidito C., Carr M. J., Tenner T. and Ozerov A. (2016) A calcium-in-olivine geohygrometer and its

- application to subduction zone magmatism. *J. Petrol.* **57**, 1811–1832.
- Giuli G., Alonso-Mori R., Cicconi M. R., Paris E., Glatzel P., Eeckhout S. G. and Scaillet B. (2012) Effect of alkalis on the Fe oxidation state and local environment in peralkaline rhyolitic glasses. Am. Mineral. 97, 468–475.
- Giuli G., Paris E., Hess K. U., Dingwell D. B., Cicconi M. R., Eeckhout S. G., Fehr K. T. and Valenti P. (2011) XAS determination of the Fe local environment and oxidation state in phonolite glasses. *Am. Mineral.* 96, 631–636.
- Giuli G., Paris E., Pratesi G., Koeberl C. and Cipriani C. (2003) Iron oxidation state in the Fe-rich layers and silica matrix of Libyan Desert Glass: a high-resolution XANES study. *Mete-orit. Planet. Sci.* 38, 1171–1186.
- Gualda G. A. R., Ghiorso M. S., Lemons R. V. and Carley T. L. (2012) Rhyolite-MELTS: a modified calibration of MELTS optimized for Silica-rich, fluid-bearing magmatic systems. *J. Petrol.* **53**, 875–890.
- Gurenko A. A., Sobolev A. V. and Kononkova N. N. (1991) Petrology of the primary magma of the Reykjanes Peninsula rift tholeittes. *Geochem. Int.* **28**, 58–71.
- Hanyu T., Shimizu K., Ushikubo T., Kimura J.-I., Chang Q., Hamada M., Ito M., Iwamori H. and Ishikawa T. (2019) Tiny droplets of ocean island basalts unveil Earth's deep chlorine cycle. *Nat. Commun.* 10, 60.
- Hartley M. E., Morgan D. J., Maclennan J., Edmonds M. and Thordarson T. (2016) Tracking timescales of short-term precursors to large basaltic fissure eruptions through Fe-Mg diffusion in olivine. *Earth Planet. Sci. Lett.* 439, 58–70.
- Hartley M. E., Neave D. A., Maclennan J., Edmonds M. and Thordarson T. (2015) Diffusive over-hydration of olivinehosted MIs. *Earth Planet. Sci. Lett.* 425, 168–178.
- Hartley M. E., Shorttle O., Maclennan J., Moussallam Y. and Edmonds M. (2017) Olivine-hosted MIs as an archive of redox heterogeneity in magmatic systems. *Earth Planet. Sci. Lett.* 479, 192–205.
- Head E., Lanzirotti A., Newville M. and Sutton S. (2018) Vanadium, sulfur, and iron valences in MIs as a window into magmatic processes: a case study at Nyamuragira volcano, Africa. Geochim. Cosmochim. Acta 226, 149–173.
- Herzberg C. (2011) Identification of source lithology in the Hawaiian and Canary Islands: implications for origins. *J. Petrol.* **52**, 113–146.
- Hickey-Vargas R., Holbik S., Tormey D., Frey F. A. and Moreno Roa H. (2016) Basaltic rocks from the Andean Southern Volcanic Zone: insights from the comparison of along-strike and small-scale geochemical variations and their sources. *Lithos* 258–259, 115–132.
- Hofmann A. W. (1988) Chemical differentiation of the Earth: the relationship between mantle, continental crust, and oceanic crust. *Earth Planet. Sci. Lett.* **90**, 297–314.
- Howarth G. H. and Büttner S. H. (2019) New constraints on archetypal South African kimberlite petrogenesis from quenched glass-rich MIs in olivine megacrysts. *Gondwana Res.* 68, 116–126.
- Irvine T. N. (1965) Chromian spinel as a petrogenetic indicator. Part I. Theory. *Canadian J. Earth Sci.* **2**, 648–671.
- Jagoutz O. and Kelemen P. B. (2015) Role of arc processes in the formation of continental crust. *Annu. Rev. Earth Planet. Sci.* 43, 363–404.
- Johnson E. R., Wallace P. J., Cashman K. V., Delgado-Granados H. and Kent A. J. R. (2008) Magmatic volatile contents and degassing-induced crystallization at Volcán Jorullo, Mexico: Implications for melt evolution and the plumbing systems of monogenetic volcanoes. *Earth Planet. Sci. Lett.* 269, 478–487.

- Jugo P. J., Wilke M. and Botcharnikov R. E. (2010) Sulphur K-edge XANES analysis of natural and synthetic basaltic glasses: Implications for S speciation and S content as a function of oxygen fugacity. *Geochim. Cosmochim. Acta* 74, 5926–5938.
- Kahl M., Chakraborty S., Pompilio M. and Costa F. (2015) Constraints on the nature and evolution of the magma plumbing system of Mt. Etna Volcano (1991–2008) from a combined thermodynamic and kinetic modelling of the compositional record of minerals. J. Petrol. 56, 2025–2068.
- Kelley K. A. and Cottrell E. (2009) Water and the oxidation state of subduction zone magmas. *Science* **325**, 605–607.
- Kelley K. A. and Cottrell E. (2012) The influence of magmatic differentiation on the oxidation state of Fe in a basaltic arc magma. *Earth Planet. Sci. Lett.* 329–330, 109–121.
- Kelley K. A., Plank T., Grove T. L., Stolper E. M., Newman S. and Hauri E. (2006) Mantle melting as a function of water content beneath back-arc basins. *J. Geophys. Res.* 111, B09208.
- Kent A. J. R. (2008) MIs in basaltic and related volcanic rocks. Rev. Mineral. Geochem. 69, 273–331.
- Knipping J. L., Behrens H., Wilke M., Göttlicher J. and Stabile P. (2015) Effect of oxygen fugacity on the coordination and oxidation state of iron in alkali bearing silicate melts. *Chem. Geol.* 411, 143–154.
- Kraft S., Stümpel J., Becker P. and Kuetgens U. (1996) High resolution X-ray absorption spectroscopy with absolute energy calibration for the determination of absorption edge energies. *Rev. Sci. Instrum.* 67, 681–687.
- Kress V. C. and Carmichael I. S. E. (1991) The compressibility of silicate liquids containing Fe<sub>2</sub>O<sub>3</sub> and the effect of composition, temperature, oxygen fugacity and pressure on their redox states. *Contrib. Miner. Petrol.* 108, 82–92.
- Laubier M., Gale A. and Langmuir C. (2012) Melting and crustal processes at the FAMOUS segment (Mid-Atlantic Ridge): new insights from olivine-hosted MIs from multiple samples. *J. Petrol.* **53**, 665–698.
- Laubier M., Grove T. L. and Langmuir C. H. (2014) Trace element mineral/melt partitioning for basaltic and basaltic andesitic melts: an experimental and laser ICP-MS study with application to the oxidation state of mantle source regions. *Earth Planet. Sci. Lett.* 392, 265–278.
- Laubier M., Schiano P., Doucelance R., Ottolini L. and Laporte D. (2007) Olivine-hosted MIs and melting processes beneath the FAMOUS zone (Mid-Atlantic-Ridge). *Chem. Geol.* **240**, 129– 150.
- Lee C.-T. A., Leeman W. P., Canil D. and Li Z.-X. A. (2005) Similar V/Sc systematics in MORB and arc basalts: implications for the oxygen fugacities of their mantle source regions. *J. Petrol.* **46**, 2313–2336.
- Lee C.-T. A., Luffi P., Le Roux V., Dasgupta R., Albaréde F. and Leeman W. P. (2010) The redox state of arc mantle using Zn/Fe systematics. *Nature* **468**, 681–685.
- Lloyd A. S., Plank T., Ruprecht P., Hauri E. H. and Rose W. (2013) Volatile loss from melt inclusions in pyroclasts of differing sizes. *Contrib. Miner. Petrol.* 165, 129–153.
- Lowenstern J. B. (1995) Application of silicate MIs to the study of magmatic volatiles. In *Magmas, fluids, and ore deposits*, 23 (ed. J. F. H. Thompson). Mineralogical Society of Canada, pp. 71–99.
- Mallmann G. and O'Neill H. S. C. (2009) The crystal/melt partitioning of V during mantle melting as a function of oxygen fugacity compared with some other elements (Al, P, Ca, Sc, Ti, Cr, Fe, Ga, Y, Zr and Nb). J. Petrol. 50, 1765–1794.
- Manzini M., Bouvier A.-S., Barnes J. D., Bonifacie M., Rose-Koga
  E. F., Ulmer P., Métrich N., Bardoux G., Williams J., Layne G.
  D., Straub S., Baumgartner L. P. and John T. (2017) SIMS

- chlorine isotope analyses in MIs from arc settings. *Chem. Geol.* **449**, 112–122.
- Martin V. M., Morgan D. J., Jerram D. A., Caddick M. J., Prior D. J. and Davidson J. P. (2008) Bang! Month-scale eruption triggering at Santorini volcano. *Science* 321, 1178.
- Mattioli G. S. and Wood B. J. (1988) Magnetite activities across the MgAl<sub>2</sub>O<sub>4</sub>-Fe<sub>3</sub>O<sub>4</sub> spinel join, with application to thermobarometric estimates of upper mantle oxygen fugacity. *Contrib. Miner. Petrol.* **98**, 148–162.
- McDonough W. F. and Sun S.-S. (1995) The composition of the earth. *Chem. Geol.* **120**, 223–253.
- Metrich N., Berry A. J., O'Neill H., St C. and Susini J. (2009) The oxidation state of sulfur in synthetic and natural glasses determined by X-ray absorption spectroscopy. *Geochim. Cosmochim. Acta* 73, 2382–2399.
- Mironov N. L. and Portnyagin M. V. (2011) H<sub>2</sub>O and CO<sub>2</sub> in parental magmas of Kliuchevskoi volcano inferred from study of melt and fluid inclusions in olivine. *Russ. Geol. Geophys.* **52**, 1353–1367.
- Moretti R. (2005) Polymerisation, basicity, oxidation state and their role in ionic modelling of silicate melts. *Ann. Geophys.* 48, 583–608.
- Morgado E., Parada M. A., Morgan D. J., Gutiérrez F., Castruccio A. and Contreras C. (2017) Transient shallow reservoirs beneath small eruptive centres: constraints from Mg-Fe interdiffusion in olivine. J. Volcanol. Geoth. Res. 347, 327– 336
- Morgan G. B. and London D. (2005) Effect of current density on the electron microprobe analysis of alkali aluminosilicate glasses. *Am. Mineral.* **90**, 1131–1138.
- Moussallam Y., Edmonds M., Scaillet B., Peters N., Gennaro E., Sides I. and Oppenheimer C. (2016) The impact of degassing on the oxidation state of basaltic magmas: a case study of Kīlauea volcano. *Earth Planet. Sci. Lett.* **450**, 317–325.
- Moussallam Y., Oppenheimer C., Scaillet B., Gaillard F., Kyle P., Peters N., Hartley M., Berlo K. and Donovan A. (2014) Tracking the changing oxidation state of Erebus magmas, from mantle to surface, driven by magma ascent and degassing. *Earth Planet. Sci. Lett.* **393**, 200–209.
- Neave D. A., Shorttle O, Oeser M., Weyer S. and Kobayashi K. (2018) Mantle-derived trace element variability in olivines and their MIs. Earth Planet. Sci. Lett. 483, 90–104.
- Nekrylov N., Portnyagin M., Kamenetsky V. S., Mironov N., Churikova T., Plechov P., Abersteiner A., Gorbach N., Gordeychik B., Krasheninnikov S., Tobelko D., Yu Shur M., Tetroeva S. A., Volynets A. O., Hoernle K. and Wörner G. (2018) Chromium spinel in Late Quaternary volcanic rocks from Kamchatka: implications for spatial compositional variability of subarc mantle and its oxidation state. *Lithos* 322, 212–224
- O'Connor J. T. (1965) A classification for quartz-rich igneous rocks based on feldspar ratios. U.S. Geological Survey Professional Paper B 525, 79–84.
- O'Neill H. S. C. and Wall V. J. (1987) The olivine-orthopyroxenespinel oxygen geobarometer, the nickel precipitation curve, and the oxygen fugacity of the Earth's upper mantle. *J. Petrol.* **28**, 1169–1191.
- O'Neill H. S. C., Berry A. J. and Mallmann G. (2018) The oxidation state of iron in Mid-Ocean Ridge Basaltic (MORB) glasses: implications for their petrogenesis and oxygen fugacities. *Earth Planet. Sci. Lett.* **504**, 152–162.
- Oppenheimer C. (2003) Volcanic degassing. *Treat. Geochem.*, 123–166.
- Pankhurst M. J., Morgan D. J., Thordarson T. and Loughlin S. C. (2018) Magmatic crystal records in time, space, and process,

- causatively linked with volcanic unrest. *Earth Planet. Sci. Lett.* **493**, 231–241.
- Papike J. J., Burger P. V., Bell A. S., Le L., Shearer C. K., Sutton S. R., Jones J. and Newville M. (2013) Developing vanadium valence state oxybarometers (spinel-melt, olivine-melt, spinel-olivine) and V/(Cr+Al) partitioning (spinel-melt) for martian olivine-phyric basalts. Am. Mineral. 98, 2193–2196.
- Parkinson I. J. and Arculus R. J. (1999) The redox state of subduction zones: insights from arc-peridotites. *Chem. Geol.* 160, 409–423.
- Paton C., Hellstrom J., Paul B., Woodhead J. and Hergt J. (2011) Iolite: Freeware for the visualization and processing of mass spectrometric data. J. Anal. At. Spectrom. 26, 2508–2518.
- Philibert J. (1991) Atom Movements, Diffusion and Mass Transport in Solids. Les éditions de Physique, Les Ulis, France, p. 577.
- Portnyagin M., Almeev R., Matveev M. and Holtz F. (2008) Experimental evidence for rapid water exchange between melt inclusions in olivine and host magma. *Earth Planet. Sci. Lett.* 272, 541–552.
- Portnyagin M., Mironov N., Botcharnikov R., Gurenko A., Almeev R. R., Luft C. and Holtz F. (2019) Dehydration of melt inclusions in olivine and implications for the origin of silica-undersaturated island-arc melts. *Earth Planet. Sci. Lett.* 517, 95–105.
- Portnyagin M. V., Plechov P. Y., Matveev S. V., Osipenko A. B. and Mironov N. L. (2005) Petrology of avachites, high-magnesian basalts of Avachinsky volcano, Kamchatka: I. General characteristics and composition of rocks and minerals. *Petrology* 13, 99–121.
- Prior D. J., Boyle A. P., Brenker F., Cheadle M. C., Day A., López G., Peruzzio L., Potts G. J., Reddy S., Spiess R., Timms N. E., Trimby P., Wheeler J. and Zetterström L. (1999) The application of electron backscatter diffraction and orientation contrast imaging in the SEM to textural problems in rocks. *Am. Mineral.* 84, 1741–1759.
- Qin Z., Lu F. and Anderson, Jr., A. T. (1992) Diffusive reequilibration of melt and fluid inclusions. Am. Mineral. 77, 565–576.
- Rea J. C., Varekamp J. C., Mandeville C., Goss A. R. and Colvin A. (2009) Regional magmatic setting of Callaqui Volcano, (S-Andes Chile). In *Abstract, Portland GSA Annual Meeting*, pp. 33–114.
- Reinhard A. A., Jackson M. G., Koornneef J. M., Rose-Koga E. F., Blusztajn J., Konter J. G., Koga K. T., Wallace P. J. and Harvey J. (2018) Sr and Nd isotopic compositions of individual olivine-hosted MIs from Hawai'i and Samoa: implications for the origin of isotopic heterogeneity in MIs from OIB lavas. *Chem. Geol.* 495, 36–49.
- Richards J. P. (2015) The oxidation state, and sulfur and Cu contents of arc magmas: implications for metallogeny. *Lithos* **233**, 27–45.
- Rowe M. C., Kent A. J. R. and Nielsen R. L. (2007) Determination of sulfur speciation and oxidation state of olivine hosted MIs. *Chem. Geol.* **236**, 303–322.
- Salas P. A., Rabbia O. M., Hernández L. B. and Ruprecht P. (2017) Mafic monogenetic vents at the Descabezado Grande volcanic field ((35.5°S-70.8°W): the northernmost evidence of regional primitive volcanism in the Southern Volcanic Zone of Chile. Int. J. Earth Sci. 106, 1107-1121.
- Schmidt M. W. and Jagoutz O. (2017) The global systematics of primitive arc melts. *Geochem. Geophys. Geosyst.* **18**, 2817–2854.
- Sellés D., Rodríguez C., Dungan M. A., Naranjo J. A. and Gardeweg M. (2004) Geochemistry of Nevado de Longaví volcano (36.2 °S): a compositionally atypical arc volcano in the Southern Volcanic Zone of the Andes. Rev. Geol. Chile 31, 293– 315.

- Shea T., Costa F., Krimer D. and Hammer J. E. (2015) Accuracy of timescales retrieved from diffusion modeling in olivine: a 3D perspective. Am. Mineral. 100, 2026–2042.
- Shimizu N. (1998) The geochemistry of olivine-hosted MIs in a FAMOUS basalt ALV519-4-1. Phys. Earth Planet. Inter. 107, 183–201.
- Shishkina T., Portnyagin M., Botcharnikov R. E., Almeev R. R., Simonyan A. V., Garbe-Schönberg D., Schuth S., Oeser M. and Holtz F. (2018) Experimental calibration and implications of olivine-melt vanadium oxybarometry for hydrous basaltic arc magmas. Am. Mineral. 103, 369–383.
- Søager N., Portnyagin M., Hoernle K., Holm P. M. and Garbe-Schönberg D. (2018) Constraints on lithosphere-asthenosphere melt mixing in basaltic intraplate volcanism from olivine melt inclusions from southern Payenia, Argentina. *Lithos* 310–311, 225–240.
- Sobolev A. V. (1996) Melt inclusions in minerals as a source of principle petrological information. *Petrology* 4, 209–220.
- Sobolev A. V. and Chaussidon M. (1996) H<sub>2</sub>O concentrations in primary melts from supra-subduction zones and mid-ocean ridges: implications for H<sub>2</sub>O storage and recycling in the mantle. *Earth Planet. Sci. Lett.* **137**, 45–55.
- Sobolev A. V., Hofmann A. W. and Kuzmin D. V., et al. (2007) The amount of recycled crust in sources of mantle-derived melts. *Science* 316, 412-417.
- Sorbadere F., Schiano P., Metrich N. and Garaebiti E. (2011) Insights into the origin of primitive silica-undersaturated arc magmas of Aoba volcano (Vanuatu arc). *Contrib. Miner. Petrol.* 162, 995–1009.
- Sovolev A. V. and Danyushevsky L. V. (1994) Petrology and geochemistry of boninites from the north termination of the tonga trench: constraints on the generation conditions of primary high-Ca boninite magmas. *J. Petrol.* **35**, 1183–1211.
- Spandler C., O'Neill H. and St C. (2010) Diffusion and partition coefficients of minor and trace elements in San Carlos olivine at 1300°C with some geochemical implications. *Contrib. Miner.* Petrol. 159, 791–818.
- Stolper D. A. and Bucholz C. E. (2019) Neoproterozoic to early Phanerozoic rise in island arc redox state due to deep ocean oxygenation and increased marine sulfate levels. *Proc. Natl. Acad. Sci.* 116, 8746–18745.
- Stolper E. and Newman S. (1994) The role of water in the petrogenesis of Mariana trough magmas. *Earth Planet. Sci. Lett.* **121**, 293–325.
- Straub S. M. and Layne G. D. (2003) The systematics of chlorine, fluorine, and water in Izu arc front volcanic rocks: implications for volatile recycling in subduction zones. *Geochim. Cosmochim. Acta* 67, 4179–4203.
- Sutton S. R., Karner J., Papike J., Delaney J. S., Shearer C., Newville M., Eng P., Rivers M. and Dyar M. D. (2005) Vanadium K edge XANES of synthetic and natural basaltic glasses and application to microscale oxygen barometry. *Geochim. Cosmochim. Acta* **69**(9), 2333–2348. https://doi.org/10.1016/j.gca.2004.10.013.
- Tang M., Erdman M., Eldridge G. and Lee C.-T. A. (2018) The redox "filter" beneath magmatic orogens and the formation of continental crust. Sci. Adv. 4, eaar4444.
- Tassara A. and Echaurren A. (2012) Anatomy of the Andean subduction one: three-dimensional density model upgraded and compared against global-scale models. *Geophys. J. Int.* 189, 161–168
- Tollan P. and Hermann J. (2019) Arc magmas oxidized by water dissociation and hydrogen incorporation in orthopyroxene. *Nat. Geosci.* **12**, 667–671.

- Volker D., Kutterolf S. and Wehrmann H. (2011) Comparative mass balance of volcanic edifices at the Southern Volcanic Zone of the Andes between 33°S and 44°S. J. Volcanol. Geoth. Res. 205, 114–129.
- Wallace P. J. (2005) Volatiles in subduction zone magmas: concentrations and fluxes based on MIs and volcanic gas data. J. Volcanol. Geoth. Res. 140, 217–240.
- Wang J., Xiong X., Takahashi E., Zhang L, Li L. and Liu X. (2019) Oxidation state of arc mantle revealed by partitioning of V, Sc, and Ti between mantle minerals and basaltic melts. J. Geophys. Res. Solid Earth 124, 4617–4638.
- Watt S. F. L., Pyle D. M., Mather T. A. and Naranjo J. A. (2013) Arc magma compositions controlled by linked thermal and chemical gradients above the subjecting slab. *Geophys. Res.* Lett. 40, 2550–2556.
- Wehrmann H., Hoernle K., Jacques G., Garbe-Schonberg D., Schuman K., Mahlke J. and Lara L. E. (2014) Volatile (sulphur and chlorine), major, and trace element geochemistry of mafic to intermediate tephras from the Chilean Southern Volcanic Zone (33–43°S). *Int. J. Earth Sci.* 103, 1945–1962.
- Weller D. J. and Stern C. R. (2018) Along-strike variability of primitive magmas (major and volatile elements) inferred from olivine-hosted MIs, southernmost Andean Southern Volcanic Zone, Chile. *Lithos* 296–299, 233–244.
- Wilke M., Partzsch G. M., Bernhardt R. and Lattard D. (2004) Determination of the iron oxidation state in basaltic glasses using XANES at the *K*-edge. *Chem. Geol.* **220**, 143–161.

- Witter J. B., Kress V. C., Delmelle P. and Stix J. (2004) Volatile degassing, petrology, and magma dynamics of the Villarica Lava Lake, Southern Chile. *J. Volcanol. Geoth. Res.* **34**, 303–337
- Wojdyr M. (2010) Fityk: a general-purpose peal fitting program. *J. Appl. Crystallogr.* **43**, 1126–1128.
- Wood B. J., Bryndzia L. T. and Johnson K. E. (1990) Mantle oxidation-state and its relationship to tectonic environment and fluid speciation. *Science* 248, 337–345.
- Woodhead J., Hellstrom J., Hergt J., Greig A. and Maas R. (2007) Isotopic and elemental imaging of geological material by laser ablation inductively coupled plasma mass spectrometry. *Geo-stand. Geoanal. Res.* 4, 331–343.
- Zajacz Z. and Halter W. (2009) Copper transport by high temperature, sulfur-rich magmatic vapor: evidence from silicate melt and vapor inclusions in a basaltic andesite from the Villarica volcano (Chile). Earth Planet. Sci. Lett. 282, 115–121.
- Zhang H. L., Cottrell E., Solheid P., Kelley K. and Hirschmann M. M. (2018) Determination of Fe<sup>3+</sup>/ΣFe of XANES basaltic glass standards by Mössbauer spectroscopy and its application to the oxidation state of iron in MORB. *Chem. Geol.* **479**, 166–175.

Associate editor: Zoltan Zajacz